

Annual Review of Fluid Mechanics

Multiscale Velocity Gradients in Turbulence

Perry L. Johnson¹ and Michael Wilczek²

¹Department of Mechanical and Aerospace Engineering, University of California, Irvine, California, USA; email: perry.johnson@uci.edu

²Theoretical Physics I, University of Bayreuth, Bayreuth, Germany; email: michael.wilczek@uni-bayreuth.de

Annu. Rev. Fluid Mech. 2024. 56:463-90

First published as a Review in Advance on October 10, 2023

The Annual Review of Fluid Mechanics is online at fluid.annualreviews.org

https://doi.org/10.1146/annurev-fluid-121021-031431

Copyright © 2024 by the author(s). This work is licensed under a Creative Commons Attribution 4.0 International License, which permits unrestricted use, distribution, and reproduction in any medium, provided the original author and source are credited. See credit lines of images or other third-party material in this article for license information.

ANNUAL CONNECT

www.annualreviews.org

- · Download figures
- Navigate cited references
- · Keyword search
- Explore related articles
- Share via email or social media

Keywords

turbulence theory, small-scale turbulence modeling, energy cascade, Lagrangian dynamics

Abstract

Understanding and predicting turbulent flow phenomena remain a challenge for both theory and applications. The nonlinear and nonlocal character of small-scale turbulence can be comprehensively described in terms of the velocity gradients, which determine fundamental quantities like dissipation, enstrophy, and the small-scale topology of turbulence. The dynamical equation for the velocity gradient succinctly encapsulates the nonlinear physics of turbulence; it offers an intuitive description of a host of turbulence phenomena and enables establishing connections between turbulent dynamics, statistics, and flow structure. The consideration of filtered velocity gradients enriches this view to express the multiscale aspects of nonlinearity and flow structure in a formulation directly applicable to large-eddy simulations. Driven by theoretical advances together with growing computational and experimental capabilities, recent activities in this area have elucidated key aspects of turbulence physics and advanced modeling capabilities.



Large-eddy simulations (LES):

unsteady computational fluid dynamics performed with a grid spacing that resolves larger-scale turbulent motions but not smaller-scale eddies that need subgrid modeling

Vortex stretching:

occurs when a vortex is subjected to an extensional strain rate along its axis of rotation, increasing the vorticity magnitude

Direct numerical simulation (DNS):

fully resolved numerical solution of the Navier–Stokes equations

1. INTRODUCTION

The phenomenon of turbulence arises in diverse scientific and engineering flows. As such, our ability to understand, predict, or manipulate turbulent flows is a key challenge of critical pursuits ranging from oceanography, atmospheric science, and climate to transportation, energy production, and even epidemiology. Despite its evident variety of manifestations, turbulence tends to produce salient and ubiquitous features, including (a) high rotationality, (b) enhanced kinetic energy dissipation rate, and (c) intrinsic multiscale structure. As a tool to probe turbulence dynamics, the velocity gradient tensor (VGT), together with its coarse-grained generalization, offers a unique advantage in its potential to connect the statistics, dynamics, and coherent structures of turbulence in a unified multiscale framework. The statistics of (coarse-grained) velocity gradients straightforwardly display the scaling and intermittency observed in both the inertial and viscous ranges of scales. The dynamics of (coarse-grained) velocity gradients, from a Lagrangian perspective, encode many of the peculiar nonlinear features of turbulence, such as the geometrical alignment tendencies that support self-amplification and the energy cascade to small scales. The multiscale coherent structures of turbulence are intuitively described by (coarse-grained) velocity gradients in terms of the fundamental rotational and dissipative nature of turbulence, for example, vortices or strain sheets at various scales. Additionally, coarse-grained velocity gradients naturally emerge as key aspects of turbulence modeling for large-eddy simulations (LES) because full computational resolution of all scales is prohibitively expensive for most applications.

The description of the multiscale structure of turbulence in terms of rotational structures has a long history that can be traced to Richardson's (1922) famous rhyme that first described the energy cascade as interactions between "big whirls," "little whirls," and "lesser whirls." Taylor (1938, p. 23) more explicitly connected vorticity dynamics with the enhancement of dissipation by using the concept of vortex stretching:

It seems that the stretching of vortex filaments must be regarded as the principal mechanical cause of the high rate of dissipation which is associated with turbulent motion.

It appears to be Onsager who first used the word "cascade" to describe this process (Eyink & Sreenivasan 2006). Onsager (1949, p. 282) synthesized his cascade phenomenology with Taylor's vortex stretching mechanism:

Since the circulation of a vortex tube is conserved, the vorticity will increase whenever a vortex tube is stretched. [...] This process tends to make the texture of the motion ever finer, and greatly accelerates the viscous dissipation.

In Onsager's view, the energy cascade is enabled by interactions of "velocity gradients which belong to wave-numbers" (p. 285) over the range of scales present in the flow. Thus, early descriptions of the energy cascade were often framed in terms of multiscale velocity gradient dynamics and, more specifically, multiscale vortex stretching.

In retrospect, it may seem strange that the early understanding of enhanced dissipation rate should have focused so much on vorticity dynamics as opposed to the full velocity gradient dynamics. Nonetheless, the centrality of vortex stretching as the mechanism of the energy cascade has been thoroughly ingrained in the minds of generations of turbulence researchers by the collective impact of these luminaries and the influential textbook by Tennekes & Lumley (1972). In fact, Betchov (1956) introduced two valuable statistical relations that more explicitly relate vorticity and strain rate in homogeneous, divergence-free flows. While they are pervasive influences on our understanding of turbulence, these works predate the emergence of powerful digital computers for direct numerical simulations (DNS), as well as modern high-resolution experimental measurements.

Along with DNS, theoretical research by Vieillefosse (1982, 1984) helped ignite the modern study of velocity gradients. He approximated their evolution along Lagrangian trajectories by neglecting viscosity and pressure Hessian anisotropy, demonstrating peculiar topological features that appear on the way to a finite-time singularity. Soon thereafter, the statistical footprint of these features was observed in DNS (Ashurst et al. 1987) and experiments (Tsinober et al. 1992). The advent of DNS also revealed the existence of coherent structures such as vortex tubes (e.g., Siggia 1981, She et al. 1990, Jiménez et al. 1993), reminiscent of analytical solutions to the Navier–Stokes equations (NSEs; e.g., Burgers 1948, Townsend 1951, Lundgren 1982). Wallace (2009) provides a helpful review of how DNS and experimental capabilities advanced our understanding of the statistics and structure of velocity gradients.

Given their theoretical and practical importance, it comes as no surprise that velocity gradient statistics have been subject to intense modeling efforts, first by Girimaji & Pope (1990). The following two decades saw an increase in efforts to model Lagrangian velocity gradients, as summarized by Meneveau (2011). Section 4 of this review highlights the significant progress in Lagrangian velocity gradient models in the years since.

With the availability of detailed DNS and experimental data, the concept of strain-rate self-amplification emerged as an alternative to vortex stretching for a mechanistic account of the energy cascade. Whereas vortex stretching (Taylor 1938, Onsager 1949) produces enstrophy via the interaction of vorticity with the strain rate, the strain-rate tensor also amplifies itself through nonlinear self-advection, the details of which are explored in the textbook by Tsinober (2009). Section 3 of this review shows how much has been learned about inertial-range physics in recent years through the use of new theoretical tools such as filtered velocity gradients and continual increases in Reynolds numbers available via DNS.

Before addressing filtered velocity gradients (Section 3) and Lagrangian modeling (Section 4), in Section 2 we introduce the basic properties and behaviors of (unfiltered) velocity gradients while summarizing recent progress in understanding their dynamics. Our review focuses specifically on advances in the years since previous treatments of these topics (Tsinober 2009, Wallace 2009, Meneveau 2011).

2. VELOCITY GRADIENTS: THE DISSIPATIVE SCALES

2.1. A Primer on Velocity Gradient Dynamics: Burgers Equation

A crucial aspect of velocity gradient dynamics is gradient self-amplification, whose essence can be illustrated with the one-dimensional (1D) Burgers equation (for reviews, see Frisch & Bec 2002, Bec & Khanin 2007):

$$\partial_t u(x,t) + u(x,t)\partial_x u(x,t) = \nu \partial_x^2 u(x,t).$$
 1.

Here, u(x, t) is the velocity field on the line and v denotes the kinematic viscosity. The inviscid case (v = 0) may be solved with the method of characteristics along Lagrangian trajectories Y(t, X) [with initial condition $Y(t_0, X) = X$], which are governed by

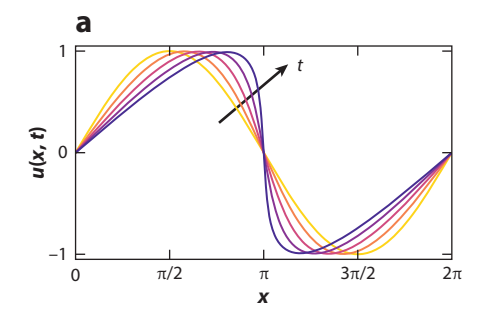
$$\frac{\mathrm{d}}{\mathrm{d}t}Y(t,X) = u\left(Y(t,X),t\right) \quad \text{and} \quad \frac{\mathrm{d}}{\mathrm{d}t}u\left(Y(t,X),t\right) = 0.$$

Lagrangian particles simply stream with a constant velocity, $Y(t, X) = X + u(X, t_0)(t - t_0)$, until their trajectories intersect, causing a shock. Considering the velocity gradient $A = \partial_x u$ along a Lagrangian trajectory yields the following gradient self-amplification equation:

$$\frac{\mathrm{d}}{\mathrm{d}t}A(Y(t,X),t) = -A(Y(t,X),t)^2, \text{ solved by } A(Y(t,X),t) = \frac{A(X,t_0)}{1 + A(X,t_0)(t-t_0)}.$$
 3.

Finite-time singularity: occurs when a gradient diverges after a finite time, corresponding to a discontinuity in a field that evolved from smooth initial conditions

Strain-rate self-amplification: specific type of gradient selfamplification due to nonlinear selfadvection in the NSE; faster-moving fluid particles tend to catch up with slower-moving ones in their path, which naturally increases the magnitude of compressive strain rates



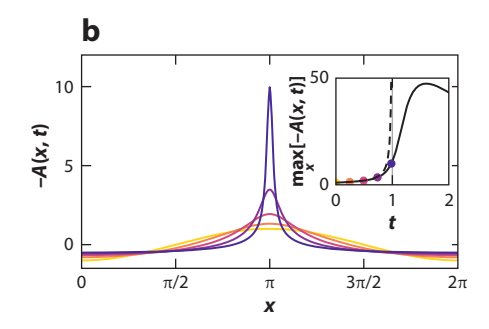


Figure 1

(a) Velocity field u(x, t) and (b) velocity gradient field A(x, t) of a numerical solution to the viscous one-dimensional Burgers equation (with v = 0.01) from an initial condition $u = \sin x$. The black arrow indicates increasing time. (*Inset*) Maximum negative gradient as a function of time (*solid line* and *dots*) compared with that of the inviscid gradient solution, A(Y(t, X), t) = A(X, 0)/(1 + A(X, 0)t) (Equation 3, *dashed line*), which exhibits a finite-time singularity at t = 1.

An initially positive velocity gradient will decay, whereas an initially negative gradient will self-amplify and eventually develop a singularity at finite time $t^* = t_0 - 1/A(X, t_0)$, corresponding to the emergence of a shock.

Viscosity regularizes these finite-time singularities (**Figure 1**). **Figure 1***a* illustrates the emergence of a steep front from a sinusoidal initial condition. **Figure 1***b* shows that the (negative) gradient increases over time but does not diverge, since it is regularized by viscous diffusion. Thus, the Burgers example presents the first indication that dynamical effects like viscous diffusion may help regularize the otherwise singular dynamics of gradient self-amplification. Clearly, the full velocity gradient dynamics in Navier–Stokes turbulence will be much richer because of three-dimensionality and the additional effects of pressure.

2.2. Velocity Gradient Dynamics

Incompressible flows are described by a three-dimensional (3D) velocity field, $\mathbf{u}(\mathbf{x}, t)$, satisfying $\nabla \cdot \mathbf{u} = 0$ and evolving according to the NSE

$$\frac{Du_i}{Dt} = -\frac{\partial p}{\partial x_i} + \nu \nabla^2 u_i + f_i,$$
4.

where $D/Dt = \partial/\partial t + \mathbf{u} \cdot \nabla$ denotes the material derivative, $p(\mathbf{x}, t)$ is the pressure (divided by density), and ν is the kinematic viscosity. The dynamics of the VGT $A_{ij} = \partial u_i/\partial x_j$ are obtained by taking the gradient of the NSE. The result is (implied summation)

$$\frac{DA_{ij}}{Dt} = -A_{ik}A_{kj} - \frac{\partial^2 p}{\partial x_i \partial x_j} + \nu \nabla^2 A_{ij} + \frac{\partial f_i}{\partial x_i}.$$
 5.

Gradient self-amplification/attenuation appears as the first term on the right-hand side, originating from the advection term in the NSE. It is the 3D equivalent of the $-A^2$ term in Equation 3. The second term is the pressure Hessian (H_{ij}) , and the third term results from the viscous term in the NSE. The last term corresponds to the gradient of any external forcing term in the NSE. Equation 5 can be interpreted as an equation for the rate of change of the velocity gradients along Lagrangian trajectories.

The VGT can be decomposed into its symmetric part, the strain-rate tensor, and its antisymmetric part, the rotation-rate tensor:

$$A_{ij} = S_{ij} + W_{ij}, S_{ij} = \frac{1}{2} (A_{ij} + A_{ji}), W_{ij} = \frac{1}{2} (A_{ij} - A_{ji}).$$
 6.

The strain-rate tensor quantifies the deformation of a local fluid element due to stretching/compression and determines the local dissipation rate, $\varepsilon = 2\nu S_{ij}S_{ij}$. The rotation-rate tensor is directly related to the vorticity pseudovector, $W_{ij} = -\epsilon_{ijk}\omega_k/2$, and therefore to the local enstrophy, $\omega^2 = -2W_{ij}W_{ji}$. Alternative decompositions have been proposed; these include the Schur decomposition (Keylock 2018), triple decomposition (Das & Girimaji 2020, Nagata et al. 2020), and Rortex-based decomposition (Gao & Liu 2019).

Equation 5 can be decomposed into the dynamics of the vorticity and the strain-rate tensor, from which we can see how their (squared) magnitudes (enstrophy and dissipation) change. Neglecting the force, we find

$$\frac{D\left(\frac{1}{2}\omega_{i}\omega_{i}\right)}{Dt} = \omega_{i}S_{ij}\omega_{j} + \nu\nabla^{2}\left(\frac{1}{2}\omega_{i}\omega_{i}\right) - \nu\frac{\partial\omega_{i}}{\partial x_{i}}\frac{\partial\omega_{i}}{\partial x_{i}},$$

$$7.$$

$$\frac{D\left(S_{ij}S_{ij}\right)}{Dt} = -2S_{ij}S_{jk}S_{ki} - \frac{1}{2}\omega_iS_{ij}\omega_j - 2S_{ij}\frac{\partial^2 p}{\partial x_i\partial x_j} + \nu\nabla^2\left(S_{ij}S_{ij}\right) - 2\nu\frac{\partial S_{ij}}{\partial x_k}\frac{\partial S_{ij}}{\partial x_k}, \qquad 8.$$

illustrating the mutual coupling of the two fields. The sum of Equations 7 and 8 gives the rate of change of $A_{ij}A_{ij} = S_{ij}S_{ij} + \omega_i\omega_i/2$.

Vortex stretching/tilting $(S_{ij}\omega_j)$, which underlies enstrophy production $(\omega_i S_{ij}\omega_j)$, can be best understood in a frame in which the strain-rate tensor is initially diagonal. Since $S_{ii}=0$ due to incompressibility, the three real eigenvalues sum up to zero. Vorticity will then be amplified along the direction of the largest eigenvalue. As a result, the vorticity vector tilts toward alignment with the eigenvector of the largest eigenvalue. However, numerics and experiments show a somewhat counterintuitive result: The vorticity aligns more often with the eigenvector corresponding to the intermediate eigenvalue (Ashurst et al. 1987, Tsinober et al. 1992), and this preferential alignment is even stronger for intense vorticity events (Buaria et al. 2020a). Xu et al. (2011) shed light on this paradoxical observation by showing that the vorticity does tend to align with the eigenvector corresponding to the largest eigenvalue when the vorticity is sampled at a time lag behind the strain rate along a Lagrangian path. The physical picture behind this observation is quite intuitive: While vorticity dynamically tends to align with the eigenvector of the largest eigenvalue, the strain eigenframe continues to evolve in time. As a result, the dynamically expected alignment can be detected under a time lag, whereas the instantaneous alignment shows the counterintuitive preferential alignment with the intermediate eigenvector.

Furthermore, Ni et al. (2014) revealed that vorticity aligns with the eigenvector of the largest eigenvalue of the (left) Cauchy–Green tensor (i.e., cumulative strain over a finite time along a Lagrangian path; see the sidebar titled Velocity Gradients and Fluid Element Deformation). In both of these observations, the Lagrangian timescale of dynamical relevance is the Kolmogorov timescale, $\tau_{\eta} = \sqrt{\nu/\langle \varepsilon \rangle}$. Providing more insight, Hamlington et al. (2008) and Buaria & Pumir (2021) used a decomposition of the Biot–Savart integral that relates strain and vorticity to demonstrate that vorticity aligns with the most extensional eigenvector when its self-induced (i.e., local) strain rate is removed.

In addition to vortex stretching, the vorticity is subjected to viscous diffusion and the antisymmetric part of the forcing. Viscous tilting of vorticity distinguishes cumulative vortex stretching from cumulative material line stretching (Holzner et al. 2010, Johnson & Meneveau 2016b), an important correction to Taylor (1938) and the naive use of Kelvin's theorem for viscous flows. Interestingly, Constantin & Iyer (2008) have generalized Kelvin's theorem to viscous flows by using a stochastic representation.

The evolution equation for the strain-rate tensor features a strain self-amplification term $(-S_{ik}S_{kj})$, which gives rise to the dissipation production term $(-2S_{ij}S_{jk}S_{ki})$ in Equation 8. In

VELOCITY GRADIENTS AND FLUID ELEMENT DEFORMATION

The strain-rate tensor, **S**, describes the instantaneous rate of deformation of a fluid element. In contrast, the cumulative deformation of a fluid element over a finite time contains information from Lagrangian history that is valuable for analyzing and modeling turbulence physics. A Lagrangian trajectory, **Y**(*t*, **X**), starting from the location **X** at time t_0 advances as d**Y**(t, **X**)/dt = d(t, **X**)/dt = d(t)/d(t). The gradient of the Lagrangian map is the deformation gradient tensor, $D_{ij} = \partial Y_i / \partial X_j$, and its evolution is determined by the velocity gradient along the Lagrangian trajectory:

$$\frac{\mathrm{d}}{\mathrm{d}t}D_{ij} = \frac{\partial u_i}{\partial Y_k} \frac{\partial Y_k}{\partial X_j} = A_{ik}D_{kj}, \quad \text{with} \quad D_{ij}(t_0) = \delta_{ij}.$$
 SB1.

The deformation gradient tensor maps an initially spherical fluid element onto an ellipsoid based on the cumulative rotation and deformation under the action of the Lagrangian velocity gradient over a finite time period. The real eigenvalues and orthonormal eigenvectors of the (left) Cauchy–Green tensor, $C_{ij} = D_{ik}D_{jk}$, characterize the ellipsoid of deformation. Its temporal evolution is given by

$$\frac{\mathrm{d}}{\mathrm{d}t}C_{ij} = A_{ik}C_{kj} + C_{ik}A_{jk},$$
 SB2.

and its formal solution may be written in terms of time-ordered exponentials of the time-integrated Lagrangian VGT.

the strain-rate eigenframe, $S_{ik}S_{kj}$ is diagonal and bears some resemblance to the quadratic self-amplification in the 1D Burgers equation (Equation 3). Furthermore, vortex stretching locally decreases the dissipation rate (Equation 8), as emphasized by Tsinober (2009). Finally, the pressure Hessian, viscous diffusion, and the symmetric part of the forcing are acting, too, leading to complex dynamics of the strain rate.

2.3. Invariants of the Velocity Gradient Tensor

Enstrophy and dissipation are examples of invariants (i.e., scalar quantities characterizing the VGT that are independent of the orientation of the coordinate system). A total of five invariants are needed to fully characterize the VGT (Meneveau 2011). To simplify the discussion even further, however, it is common to consider the second and third principal invariants of the VGT (the first principal invariant is zero due to incompressibility):

$$Q = -\frac{1}{2}A_{ik}A_{ki} = \frac{1}{4}\omega_i\omega_i - \frac{1}{2}S_{ij}S_{ij}, \qquad R = -\frac{1}{3}A_{ij}A_{jk}A_{ki} = -\frac{1}{3}S_{ij}S_{jk}S_{ki} - \frac{1}{4}\omega_iS_{ij}\omega_j.$$
 9.

Q expresses the balance of enstrophy and strain-rate-squared magnitude (**Figure 2**), whereas R expresses the balance between enstrophy production (vortex stretching) and dissipation production (strain self-amplification) (Equations 7 and 8). Thus, a good deal of information about the velocity gradient can be captured by its position in QR space (depicted schematically in **Figure 3**a).

Both Q and R can be written as the divergences of a vector; therefore, their averages vanish for homogeneous flows (Betchov 1956). In particular, $\langle Q \rangle = 0$ has the consequence that average enstrophy is equal to the average strain-rate-squared magnitude, and $\langle R \rangle = 0$ means that average strain production is directly proportional to average enstrophy production. One consequence is that the net (local and nonlocal) effect of vortex stretching is to enhance the global dissipation rate (Carbone & Bragg 2020), even though it locally decreases it (as a sink in Equation 8) (Tsinober 2009). While additional Betchov constraints have been sought for a long time,

Betchov constraints: statistical equalities for VGT invariants in homogeneous turbulence that are a consequence of incompressibility (solenoidal velocity field)

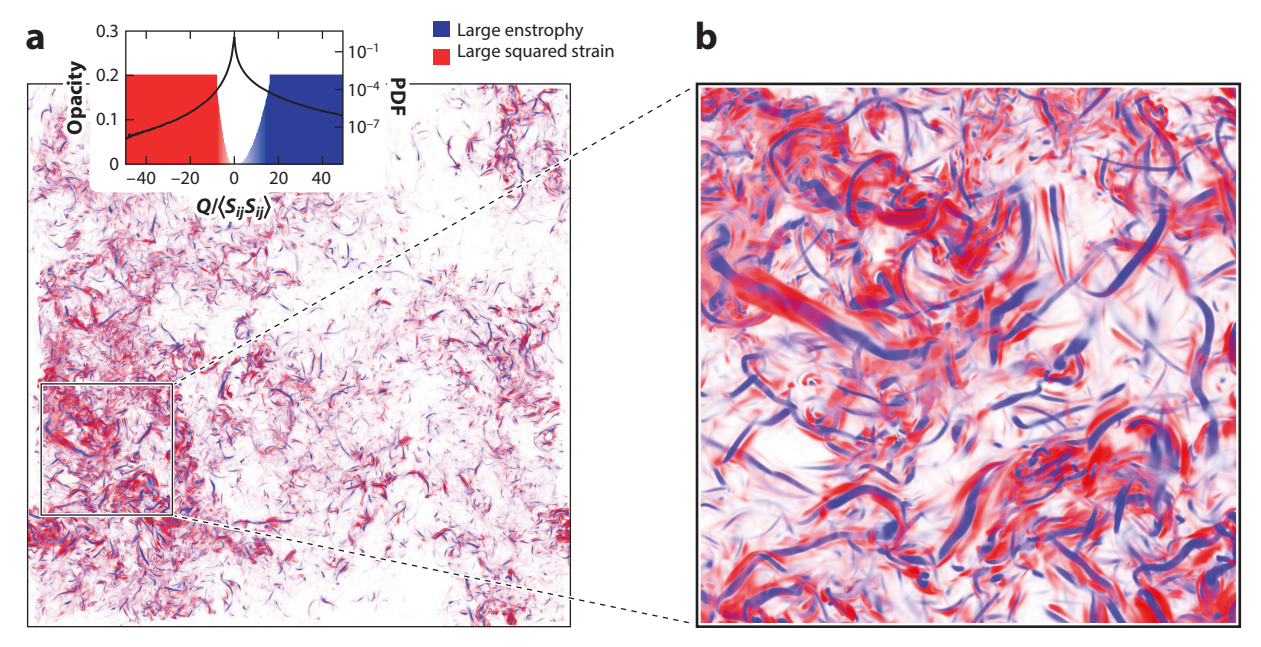


Figure 2

(a) Visualization of large enstrophy (blue) and large squared strain (red) by means of the second invariant Q from a simulation of homogeneous isotropic turbulence ($Re_{\lambda} \approx 280$). (b) Zoomed-in view of the boxed region in panel a. Since these strong events are spatially colocalized, their contribution to the pressure partially cancels (Equation 10). Abbreviation: PDF, probability density function. Figure provided by Cristian C. Lalescu.

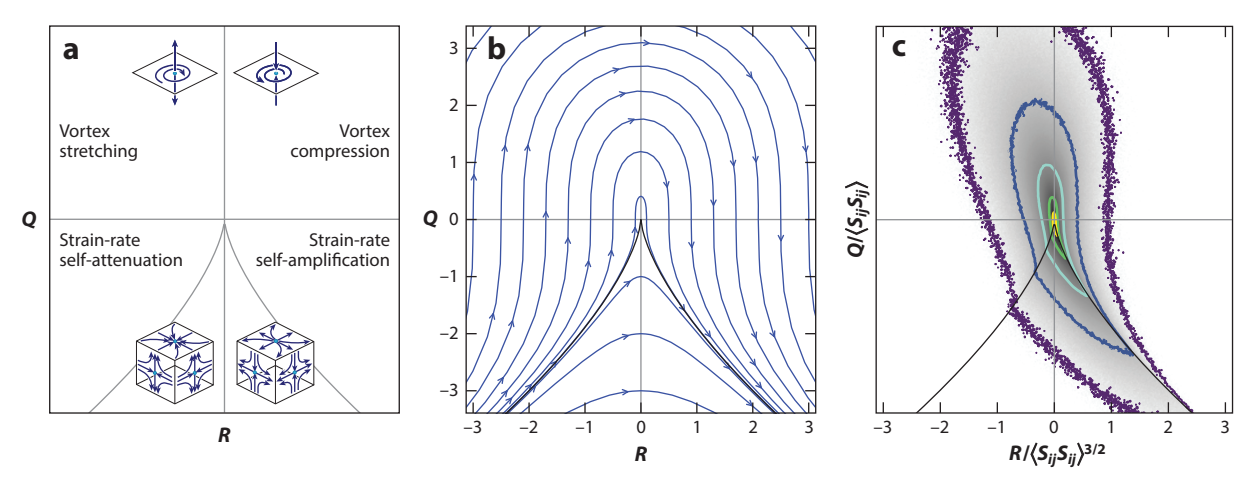


Figure 3

(a) Qualitative description of the QR space in terms of the dominant gradient amplification (or attenuation) mechanism in each quadrant. (b) QR-space trajectories of the restricted Euler system (Equation 14). (Almost) all initial conditions experience a finite-time singularity dominated by strain-rate self-amplification in the lower-right quadrant. (c) Joint PDF of Q and R from DNS of HIT at $Re_{\lambda} \approx 420$ (Li et al. 2008), whose asymmetry can be associated with the restricted Euler dynamics. Abbreviations: DNS, direct numerical simulations; HIT, homogeneous, isotropic turbulence; PDF, probability density function. Figure adapted with permission from Johnson & Meneveau (2017a); copyright Cambridge University Press.

Carbone & Wilczek (2022) recently suggested that the two Betchov constraints are the only possible ones for homogeneous isotropic turbulence.

The Betchov constraints relate averages of enstrophy and dissipation, but the gradient self-amplification mechanisms tend to generate intermittent extreme events. The related non-Gaussianity increases with Reynolds number. Recent growth in computing power has led to unprecedented access to extreme events (Ishihara et al. 2009, Yeung et al. 2015, Buaria et al. 2019, Yeung & Ravikumar 2020), which appear to have their own peculiar features (see also **Figure 2**). Some studies have identified real-space structures smaller than the Kolmogorov scale, while other studies have used a spectral approach to examine the far-dissipation range of scales (Schumacher 2007, Khurshid et al. 2018, Buaria & Sreenivasan 2020, Buaria & Pumir 2022).

2.4. Relation to the Pressure Field

The trace of Equation 5 yields the pressure Poisson equation $\nabla^2 p = 2Q$, so the trace of the pressure Hessian can be expressed in terms of the local velocity gradient. Equation 9 shows that the local pressure concavity can be further expressed in terms of the difference between the enstrophy and the squared strain (**Figure 2**). For 3D unbounded domains, the pressure is then given by

$$p(\mathbf{x},t) = -\frac{1}{2\pi} \int d\mathbf{x}' \frac{Q(\mathbf{x}',t)}{|\mathbf{x} - \mathbf{x}'|}.$$
 10.

This relation suggests an analogy with electrostatics, where the electrostatic potential is determined by a (weighted) integration of the charge density over the whole space (e.g., Douady et al. 1991, Nelkin 1994, Pumir 1994). Contributions from (colocalized) positive and negative electric charges can cancel in this integral, which can give rise to a screening effect like that observed, for example, when adding a test charge to an otherwise neutral plasma (for a turbulence-related discussion, see Davidson 2011 and references therein). From the Betchov constraints we know that the enstrophy and the squared strain on average balance each other, suggesting that cancellations of the two fields play a role in determining the pressure from the velocity gradient field. This idea was recently confirmed by Vlaykov & Wilczek (2019), who showed that, depending on the local flow conditions, the velocity gradient contributions to the pressure may come from a neighborhood that is more local than naively expected on the basis of the nonlocal expression in Equation 10.

The nonlocality of the pressure complicates velocity gradient dynamics. One can regroup the nonlinear and pressure terms in Equation 5 into local (velocity gradient self-amplification and isotropic pressure effects) and nonlocal (deviatoric pressure effects) contributions:

$$A_{ik}A_{kj} + \frac{\partial^2 p}{\partial x_i \partial x_j} = \underbrace{\left(A_{ik}A_{kj} - \frac{1}{3}A_{mn}A_{nm}\delta_{ij}\right)}_{\text{local}} + \underbrace{\left(\frac{\partial^2 p}{\partial x_i \partial x_j} - \frac{1}{3}\nabla^2 p \,\delta_{ij}\right)}_{\text{nonlocal }\widetilde{H}_{ij}}.$$
 11.

The nonlocal (deviatoric) part of the pressure Hessian \widetilde{H}_{ij} can be obtained from taking second spatial derivatives of Equation 10 (Ohkitani & Kishiba 1995):

$$\widetilde{H}_{ij}(\mathbf{x},t) = \frac{1}{2\pi} \int_{\text{P.V.}} d\mathbf{x}' \left[\frac{\delta_{ij}}{|\mathbf{x} - \mathbf{x}'|^3} - 3 \frac{(x_i - x_i')(x_j - x_j')}{|\mathbf{x} - \mathbf{x}'|^5} \right] Q(\mathbf{x}',t),$$
 12.

where P.V. denotes the principal value of the integral. Thus, the pressure Hessian at a single point depends on the variation of *Q* around that point. Like the NSE, the velocity gradient equation is therefore a nonlinear and nonlocal integro-differential equation. As we discuss in Section 4, the nonlocal pressure Hessian contributions represent a key challenge in developing low-dimensional stochastic models for velocity gradients.

2.5. Restricted Euler

Analogous to the 1D inviscid Burgers equation, the restricted Euler equation introduced by Vieillefosse (1982, 1984) provides a convenient conceptual model for exploring gradient self-amplification in 3D solenoidal velocity fields. It is obtained by considering the VGT evolution along Lagrangian trajectories and neglecting the viscous and nonlocal pressure Hessian terms in Equation 5, leaving purely autonomous dynamics for the VGT on each path line:

$$\frac{\mathrm{d}A_{ij}}{\mathrm{d}t} = -A_{ik}A_{kj} + \frac{1}{3}A_{mn}A_{nm}\delta_{ij}.$$
13.

A remarkable property of the model is that its dynamics can be reduced to those of the two principal invariants of the velocity gradient,

$$\frac{\mathrm{d}Q}{\mathrm{d}t} = -3R, \qquad \frac{\mathrm{d}R}{\mathrm{d}t} = \frac{2}{3}Q^2, \tag{14}$$

which feature an integral of motion $(27/4)R(t)^2 + Q(t)^3 = \text{const.}$ One can see from Equation 14 that R(t) is a strictly increasing function of time (for $Q \neq 0$), so the integral of motion indicates that the system (generically) diverges over time in both variables. Vieillefosse (1982) showed that this singularity occurs in a finite time, similar to the divergence of the 1D inviscid Burgers equation outlined in Section 2.1. Empirically, velocity gradients in fluid turbulence do not diverge, so the neglected pressure and viscous terms must be responsible for preventing singular behavior. Many features that can be proven for restricted Euler (Vieillefosse 1982, 1984; Cantwell 1992) can be qualitatively confirmed in statistical biases of real turbulent flows. Examples include two positive strain-rate eigenvalues and one negative eigenvalue (Lund & Rogers 1994), alignment of vorticity with the intermediate strain-rate eigenvector (Ashurst et al. 1987), and the tendency to produce extreme velocity gradients lying along the R > 0 half of the manifold defined by $(27/4)R^2 + Q^3 = 0$. The latter tendency is evident in the consistent asymmetrical teardrop shape of the joint probability density function (PDF) of the Q and R invariants in both experimental and numerical results (**Figure 3**). The restricted Euler equation thus provides a useful qualitative tool for interpreting the impact of gradient self-amplification in turbulence.

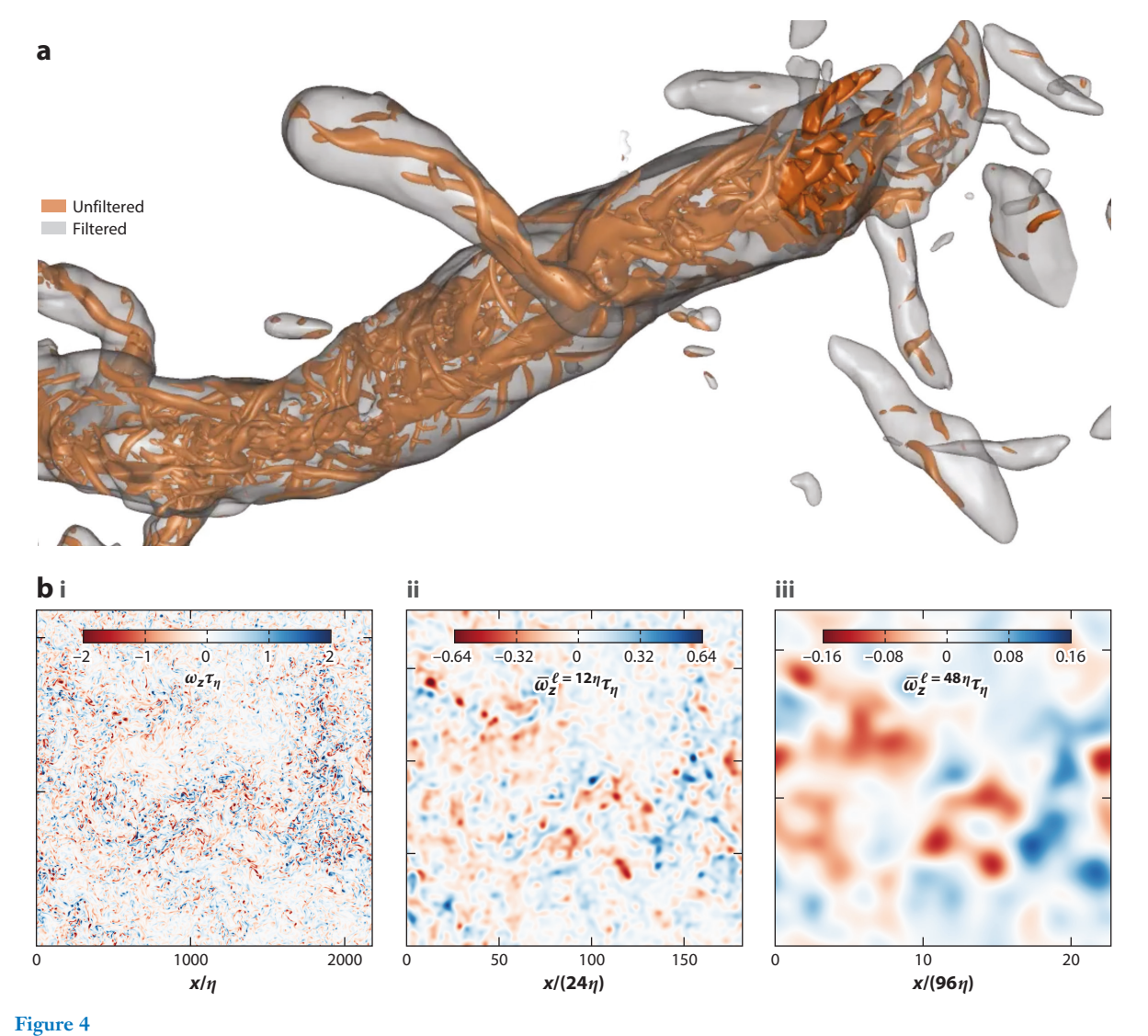
3. FILTERED VELOCITY GRADIENTS: INTERMEDIATE SCALES

3.1. Properties of Filtered Velocity Gradients

Unfiltered, the velocity gradient highlights the smallest scales of motion. The filtered velocity field and its gradient are defined using a localized spatial average (Germano 1992),

$$\overline{u}_i^{\ell}(\mathbf{x}) = \iiint_{-\infty}^{\infty} G_{\ell}(\mathbf{r}) \, u_i(\mathbf{x} + \mathbf{r}) \, \mathrm{d}\mathbf{r}, \qquad \overline{A}_{ij}^{\ell} = \frac{\partial \overline{u}_i^{\ell}}{\partial x_i},$$
 15.

where G_ℓ is the filter kernel function with characteristic width ℓ . Defined this way, filtered velocity gradients capture the spirit of Richardson's "big, little, and lesser whirls" and Onsager's "velocity gradients which belong to wave-numbers," providing a scalewise characterization of flow topology, with adjustable length scale ℓ , that maintains a spatial description of the fluid physics. For example, whirls or vortices at any intermediate scale can be identified using the second invariant of the filtered VGT, $Q^\ell = -\overline{A}_{ij}^\ell \overline{A}_{ji}^\ell/2$ (**Figure 4a**). In addition, filtered velocity gradients can be used to investigate turbulence dynamics in a formulation directly applicable to LES, an increasingly popular turbulence modeling framework (Meneveau & Katz 2000, Moser et al. 2021).



(a) Visualization of smaller vortices interacting with a larger vortex in HIT at $Re_{\lambda} \approx 420$ (Li et al. 2008) using an isosurface of the second invariant of the unfiltered (*red/bronze*) and filtered (*gray*) velocity gradient tensor. The reader is encouraged to watch the entire video provided by Bürger et al. (2012) to appreciate the beauty of multiscale velocity gradient interactions. (b) Out-of-plane vorticity on a 2D slice of a 3D HIT simulation at $Re_{\lambda} \approx 400$, both unfiltered (i) and filtered using a Gaussian kernel width of $2\ell = 24\eta$ (ii) and $2\ell = 96\eta$ (iii). The extent of the three images is the same, but the axis labels are changed to show the filter scale; the factor of 2 in 2ℓ comes from the relation to velocity increments (Equation SB3). Abbreviation: HIT, homogeneous, isotropic turbulence. Panel a reproduced with permission from Bürger et al. (2012).

3.2. Dynamics of Filtered Velocity Gradients and Kinetic Energy

The gradient of the filtered NSE describes the evolution of filtered velocity gradients,

$$\frac{\overline{D}\,\overline{A}_{ij}^{\ell}}{\overline{Dt}} = -\overline{A}_{ik}^{\ell}\overline{A}_{kj}^{\ell} - \frac{\partial^{2}\overline{p}^{\ell}}{\partial x_{i}\partial x_{j}} + \nu\nabla^{2}\overline{A}_{ij}^{\ell} - \frac{\partial^{2}\tau_{ik}^{\ell}}{\partial x_{j}\partial x_{k}} + \frac{\partial\overline{f}_{i}^{\ell}}{\partial x_{j}},$$

$$16.$$

where $\overline{D}/\overline{Dt}=\partial/\partial t+\overline{\mathbf{u}}^\ell\cdot\nabla$ is the material derivative featuring the filtered velocity field. The second derivative of $\tau_{ij}^\ell=\overline{u_iu_j}^\ell-\overline{u}_i^\ell\overline{u}_j^\ell$, the residual stress tensor, captures how smaller-scale motions affect the filtered gradient. The other terms in Equation 16 correspond to those in the unfiltered gradient dynamics in Equation 5. In particular, gradient self-amplification (vortex stretching and strain-rate self-amplification) is an important aspect of filtered dynamics.

Spatial filtering conveniently separates a flow's total kinetic energy into large-scale energy (that which is resolved at scale ℓ), $K^{\ell} = \overline{u}_{i}^{\ell} \overline{u}_{i}^{\ell}/2$, and small-scale energy (that which is removed by the filter), $k^{\ell} = \tau_{ii}/2$. The dynamical equations for K^{ℓ} and k^{ℓ} are straightforwardly derived from the NSE:

$$\frac{\partial K^{\ell}}{\partial t} + \frac{\partial \Phi_{j}^{\ell}}{\partial x_{i}} = \overline{u}_{i}^{\ell} \overline{f}_{i}^{\ell} - 2\nu \overline{S}_{ij}^{\ell} \overline{S}_{ij}^{\ell} - \Pi^{\ell},$$
 17.

$$\frac{\partial k^{\ell}}{\partial t} + \frac{\partial \phi_{j}^{\ell}}{\partial x_{j}} = \tau^{\ell}(u_{i}, f_{i}) - 2\nu\tau^{\ell}\left(S_{ij}, S_{ij}\right) + \Pi^{\ell},$$
18.

where Φ_j^ℓ and ϕ_j^ℓ represent their respective net-zero spatial fluxes and the notation for the generalized second moment is $\tau^\ell(a,b) = \overline{ab}^\ell - \overline{a}^\ell \overline{b}^\ell$ (for details, see, e.g., Germano 1992, Johnson 2021). The local exchange rate between large- and small-scale kinetic energy,

$$\Pi^{\ell} = -\tau_{ij}^{\ell} \overline{S}_{ij}^{\ell},$$
 19.

quantifies the kinetic energy cascade rate across scale ℓ at position \mathbf{x} and time t. Equation 19 may be interpreted as the work done by the larger-scale strain rate on the smaller-scale motions (Tennekes & Lumley 1972, Ballouz & Ouellette 2018).

In the inertial range of scales, $\eta \ll \ell \ll L$, assuming approximate local homogeneity, $\langle \Pi^{\ell} \rangle \approx \langle \varepsilon \rangle$. This relation between an inertial-range quantity and the dissipation rate stands in close analogy to the Kolmogorov (1941a) four-fifths law, namely $-5/(4r)\langle (\delta u_r)^3 \rangle \approx \langle \varepsilon \rangle$, where δu_r denotes the longitudinal velocity increment over scale r. Following Kolmogorov's arguments (commonly abbreviated as K41), the magnitude of filtered velocity gradients may be estimated as $\|\overline{\mathbf{A}}^{\ell}\| \sim \ell^{-2/3}$ (for more details, see the sidebar titled Structure Functions, Energy Spectra, and Velocity Gradients).

3.3. Scale Dependence of Filtered Velocity Gradients

The prominent effects of filtering velocity gradients at scale ℓ can mostly be accounted for by rescaling according to a scale-dependent timescale, $\tau_{\ell} = \langle \| \overline{\mathbf{A}}^{\ell} \|^2 \rangle^{-1/2} \sim \ell^{2/3}$, especially if one separately considers the viscous and inertial ranges. Scaled in this way, the characteristic teardrop shape of probability in the QR plane changes very little as a function of filter width within the inertial range (Lozano-Durán et al. 2016, Danish & Meneveau 2018; earlier evidence is given in Borue & Orszag 1998, van der Bos et al. 2002). The asymmetric shape of the QR PDF is lost as the filtered velocity gradients become Gaussian near the integral length scale (Naso & Pumir 2005). Between the viscous and inertial scales, the forces responsible for determining the details change significantly, as the influence of viscosity fades for $\ell \gg \eta$ and is largely replaced by the residual stress term, $\partial^2 \tau_{ik}^{\ell}/\partial x_j \partial x_k$. The effects of the viscous and residual forces on the dynamics projected to the QR plane are largely similar, with some slight differences (Danish & Meneveau 2018). As in the unfiltered case (e.g., **Figure 3**), gradient self-amplification remains a salient influence on filtered velocity gradient dynamics in the inertial range. The scalewise differences in filtered velocity gradient statistics are most evident in terms of skewness and intermittency in higher-order

STRUCTURE FUNCTIONS, ENERGY SPECTRA, AND VELOCITY GRADIENTS

Kolmogorov (1941b) used velocity increments, $\delta u_i(\mathbf{r}; \mathbf{x}) = u_i(\mathbf{x} + \mathbf{r}) - u_i(\mathbf{x})$, to express his similarity hypotheses. A major focus of turbulence theory has been the determination of inertial-range scaling exponents, ζ_p , for *p*th-order structure functions that scale as $\langle (\delta u)^p \rangle \sim |\mathbf{r}|^{\zeta_p}$ (Frisch 1995). Filtered velocity gradients are actually local averages of velocity increments (Eyink 1995):

$$\overline{A}_{ij}^{\ell}(\mathbf{x}) = -\iiint_{-\infty}^{\infty} \frac{\partial G_{\ell}}{\partial r_{j}}(\mathbf{r}) \, \delta u_{i}(\mathbf{r}, \mathbf{x}) \, \mathrm{d}\mathbf{r}.$$
 SB3.

Filtered velocity gradients have the added benefit of smoothing out the influence of scales much smaller than ℓ . A rigorous inequality based on Equation SB3 implies that $\langle \|\overline{\mathbf{A}}^{\ell}\|^p \rangle \sim \ell^{\zeta_p - p}$. When this relation is combined with inequalities for the residual stress, it follows that $\langle \Pi^{\ell} \rangle \sim \ell^{\zeta_3 - 1}$, which, together with $\langle \Pi^{\ell} \rangle \approx \langle \varepsilon \rangle$, leads to $\zeta_3 = 1$, the same result as the Kolmogorov (1941a) four-fifths law (Eyink 2007; see also Dubrulle 2019).

The filtered velocity gradient variance can be written in terms of the energy spectrum,

$$\left\langle \|\overline{\mathbf{A}}^{\ell}\|^{2}\right\rangle = 2 \int_{0}^{\infty} k^{2} \widehat{G}_{\ell}^{2}(k) E(k) \, \mathrm{d}k,$$
 SB4.

where \widehat{G}_{ℓ} is proportional to the filter kernel's Fourier transform. $\widehat{G}_{\ell} = 1$ for $k\ell \ll 1$ and rapidly decreases to zero for $k\ell > 1$, so the filtered velocity gradient variance is dominated by wave numbers near $k = \ell^{-1}$ according to the inertial-range estimate $E(k) \sim k^{-5/3}$. Therefore, $\langle \|\overline{\mathbf{A}}^{\ell}\|^2 \rangle \sim \ell^{-4/3}$; in other words, $\zeta_2 \approx 2/3$. Thus, the filtered velocity gradient is intimately connected to classical tools such as structure functions and their related theories and results.

moments, which increase with decreasing scale—qualitatively similar to the effect of Reynolds number on unfiltered gradients. Tom et al. (2021) provide a comprehensive analysis of the scale dependency of the terms involved in the filtered velocity gradient evolution (Equation 16) written in the filtered strain-rate eigenframe.

3.4. Vortex Stretching and the Cascade

The strain rate at scale ℓ will amplify (stretch) vorticity at another scale ℓ' more than it will attenuate (compress) it if $\langle \overline{\omega}_i^{\ell'} \overline{S}_{ij}^{\ell} \overline{\omega}_j^{\ell'} \rangle > 0$, which depends on the alignment of the vorticity vector with strain-rate eigenvectors and the associated eigenvalues. As mentioned above, at the smallest scales $(\ell = \ell' \lesssim \eta)$, vorticity preferentially aligns with the eigenvector of the intermediate eigenvalue, which tends to be positive more than negative (Ashurst et al. 1987, Lund & Rogers 1994). Even though not statistically well aligned, the largest positive strain-rate eigenvalue is responsible for the largest share of enstrophy production (Gulitski et al. 2007). This is also true at intermediate scales, when vorticity and strain rate are filtered at the same scale, $\ell' = \ell \gg \eta$ (Fiscaletti et al. 2016, Doan et al. 2018).

In contrast, smaller-scale vorticity aligns with the most extensional eigenvector of the larger-scale strain rate, that is, when $\ell' < \ell$ (Leung et al. 2012, Fiscaletti et al. 2016, Lozano-Durán et al. 2016). Presumably, this alignment is related to the observation by Xu et al. (2011) that (unfiltered) vorticity tends to align with the most extensional (unfiltered) strain-rate eigenvector of the time-delayed strain-rate tensor, and the observation by Hamlington et al. (2008) and Buaria & Pumir (2021) that vorticity preferentially aligns with the most extensional eigenvector of the nonlocal strain rate determined by the Biot–Savart integral. The larger-scale strain rate evolves on a slower timescale, so the smaller-scale vorticity has time to catch up to its most extensional eigenvalue, unlike the single-scale dynamics described by Xu et al. (2011). Furthermore, the larger-scale strain

rate will tend to include much more of the nonlocal strain rate compared with small-scale vorticity and, thus, should inherit the alignment statistics observed by Hamlington et al. (2008) and Buaria & Pumir (2021). Therefore, vortex stretching is more prevalent than compression at all intermediate scales of turbulence, and alignments of smaller-scale vorticity are even more biased toward the stretching direction of the larger-scale strain rate. In fact, Doan et al. (2018) found that the predominant vortex stretching interactions in turbulence were due to a strain rate at a scale three to five times larger than the vorticity filter width (i.e., $\ell = 3-5\ell'$).

The precise relationship between the cascade rate across scale ℓ (Π^{ℓ} in Equation 19) and the filtered VGT at various scales is of considerable interest for connecting known velocity gradient behaviors with energy dynamics. The filtered strain rate at scale ℓ appears explicitly in Equation 19, but the connection between the residual stress tensor and filtered velocity gradients is also required. The nonlinear gradient model of Clark et al. (1979), $\tau^{\ell}_{ij} \approx c \ell^2 \overline{A}^{\ell}_{ik} \overline{A}^{\ell}_{jk}$, represents the first term in an infinite series expansion and is highly correlated with the actual residual stress (Borue & Orszag 1998). The implied energy cascade rate is

$$\Pi^{\ell} \approx c\ell^{2} \left(\frac{1}{4} \overline{\omega}_{i}^{\ell} \overline{S}_{ij}^{\ell} \overline{\omega}_{j}^{\ell} - \overline{S}_{ij}^{\ell} \overline{S}_{jk}^{\ell} \overline{S}_{ki}^{\ell} \right) + \text{higher-order terms,}$$
 20.

where the leading term is due to this model, in which ϵ is a coefficient determined by the specific shape of the filter kernel. The leading-order term in this infinite series expansion of the cascade rate is a sum of enstrophy production (vortex stretching) and dissipation production (strain-rate self-amplification). The importance of strain-rate self-amplification for the energy cascade has been more widely recognized in recent decades (Tsinober 2009). Just as the strain rate tends to amplify vorticity, it also undergoes a self-amplification (or self-attenuation) process due to nonlinear advection, as discussed above in reference to Equation 8. The basic phenomenon of strain-rate self-amplification can be appreciated by considering again the 1D Burgers equation (Equation 1), which amplifies negative gradients (i.e., compressive strain rate; see Equation 3). The same basic effect happens in Navier–Stokes turbulence, leading to a scalewise energy transfer similar to vortex stretching (**Figure 5**).

The Betchov constraint $\langle R^{\ell} \rangle = 0$ shows that $\langle \overline{\omega}_i^{\ell} \overline{S}_{ij}^{\ell} \overline{\omega}_j^{\ell} \rangle / 4 = -\langle \overline{S}_{ij}^{\ell} \overline{S}_{ki}^{\ell} \rangle / 3$ for locally homogeneous turbulence at scale ℓ . Thus, to first-order approximation, the cascade rate can be attributed mostly to strain-rate self-amplification (75%); the contribution of vortex stretching appears

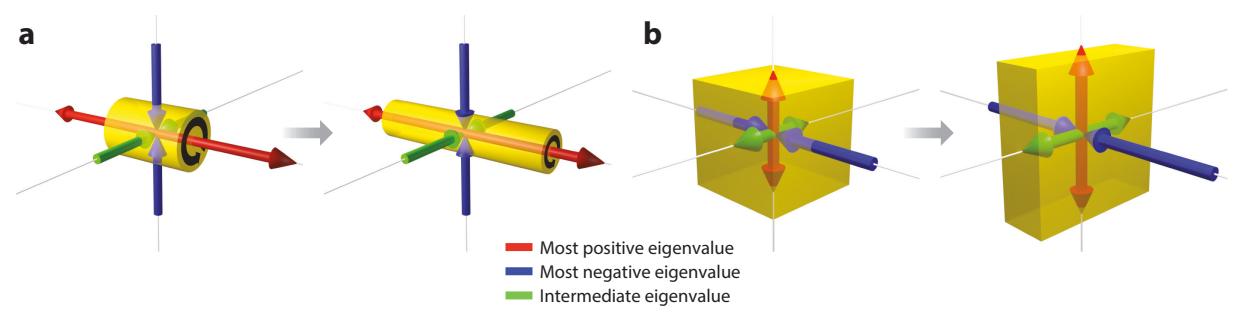


Figure 5

Schematic visualization of vortex stretching and strain self-amplification. (a) Vorticity (indicated by a yellow fluid element), which is aligned with the eigenframe of the strain-rate tensor, is stretched along the direction of the eigenvector corresponding to the most positive eigenvalue (red) and is compressed in the two other directions [i.e., eigenvectors corresponding to the most negative eigenvalue (blue) and the intermediate eigenvalue (green)]. (b) In a straining region, the negative eigenvalue self-amplifies similarly to the gradient in the 1D Burgers equation, accompanied by a compression of a fluid element (yellow) in the corresponding direction. Both dynamical effects contribute to scalewise energy transfer by generating smaller-scale structures. Figure provided by Lukas Bentkamp.

Vortex thinning:

a strain rate flattens a circular vortex to an elliptical shape, resulting in energy transfer from the vortex to the strain rate

Energy cascade
efficiency: the percent
energy cascade rate
relative to the total
rate possible if the
eigenvectors of the
strain-rate and residual
stress tensors were
perfectly aligned

weaker (25%) in this approximation. Eyink (2006) built a multiscale gradient expansion model for the residual stress based on band-pass filtering that generalized Equation 20, with leading-order terms showing the same three-to-one ratio of strain self-amplification to vortex stretching in terms of contributions to the energy cascade. More recently, Carbone & Bragg (2020) used the equation for velocity increment dynamics (de Kármán & Howarth 1938, Hill 2001), with truncation of an infinite series, to arrive at an equation very similar to Equation 20. They similarly concluded that 75% of the cascade rate is due to strain self-amplification and only 25% is due to vortex stretching. The fundamental agreement between filtering-based and increment-based methods again highlights the analogy between filtered gradients and velocity increments. However, the common reliance on truncating an infinite series expansion leaves some room for doubt as to the role of higher-order terms.

To this end, Johnson (2020, 2021) demonstrated that the residual stress tensor for Gaussian filters with scale ℓ can be written in terms of filtered velocity gradients at ℓ and all smaller scales $\ell' < \ell$ without the need to truncate an infinite series expansion. This result provides an exact relationship between the energy cascade rate across scale ℓ and multiscale velocity gradients at $\ell' \leq \ell$. Thus, the cascade rate can be written as the sum of five terms: $\Pi^{\ell} = \Pi_{\ell 1}^{\ell} + \Pi_{\ell 2}^{\ell} + \Pi_{\ell 3}^{\ell} + \Pi_{\ell 4}^{\ell} + \Pi_{\ell 3}^{\ell} + \Pi_{\ell 3}^{\ell} + \Pi_{\ell 4}^{\ell} + \Pi_{\ell 3}^{\ell} + \Pi_{\ell 4}^{\ell} + \Pi_$ $\Pi_{\omega 2}^{\ell} + \Pi_{c2}^{\ell}$. Here, $\Pi_{s1}^{\ell} = -\ell^2 \overline{S}_{ii}^{\ell} \overline{S}_{ik}^{\ell} \overline{S}_{ki}^{\ell}$ quantifies the cascade rate due to single-scale strain-rate selfamplification at ℓ , and $\Pi_{\omega l}^{\ell} = \ell^2 \overline{\omega}_i^{\ell} \overline{S}_{ij}^{\ell} \overline{\omega}_i^{\ell} / 4$ represents the cascade rate from single-scale vortex stretching at ℓ . The remaining three terms represent multiscale interactions. The strain rate at scale ℓ amplifies the strain rate and vorticity at scale $\ell' < \ell$, giving rise to the Π_{s2} and $\Pi_{\omega 2}$ portions of the cascade rate. The final term, Π_{c2} , can be thought of as a cascade rate due to vortex thinning by larger-scale strain rate. Vortex thinning (Π_{ℓ}^{ℓ}) has a negligible contribution to the average cascade rate in three dimensions for ℓ in the inertial range (Johnson 2020). However, it is the only one of the five terms that does not vanish for two dimensions—so it must represent the mechanism of the two-dimensional (2D) inverse energy cascade (Johnson 2021). The energy cascade is therefore directly expressed as the sum of multiscale strain self-amplification and vortex stretching, with the former $(\Pi_{s1}^{\ell} + \Pi_{s2}^{\ell})$ providing $\sim 5/8$ and the latter $(\Pi_{\omega 1}^{\ell} + \Pi_{\omega 2}^{\ell})$ supplying the remaining $\sim 3/8$ on the basis of DNS evidence. The contribution of vortex stretching is predominantly from multiscale interactions $(\Pi_{\omega^2}^{\ell})$ rather than the single-scale term (Π_{ω^1}) , consistent with evidence from Doan et al. (2018). Yang et al. (2023) built on Johnson's (2020, 2021) analysis by using a generalized multiscale Betchov relation to provide analytical arguments for $\langle \Pi_{s1} + \Pi_{s2} \rangle > \langle \Pi_{\omega 1} + \Pi_{\omega 2} \rangle$.

Note that this line of research mostly describes the average cascade. Carbone & Bragg (2020) found that vortex stretching plays a stronger role in fluctuations and intermittency in the cascade. The use of conditional statistics (e.g., Buaria et al. 2020b) may prove fruitful for further examination of cascade fluctuations.

3.5. Efficiency of the Cascade

Ballouz & Ouellette (2018) pointed out that Equation 19 is an inner product of two symmetric tensors, so the energy cascade rate depends not only on the magnitude of the strain-rate and stress tensors but also on the relative alignment of their (orthogonal) eigenvectors. In fact, analyses of DNS data demonstrate that the average energy cascade efficiency of such alignment is less than 50% (Ballouz & Ouellette 2018, Ballouz et al. 2020). Johnson (2021) computed the efficiency of each of the five terms in the exact decomposition of the cascade rate. The cascade efficiency of single-scale mechanisms, Π_{s1}^{ℓ} and $\Pi_{\omega1}^{\ell}$, is even lower than the total cascade efficiency. However, the multiscale versions of strain-rate self-amplification and vortex stretching show efficiencies above 70%, consistent with previous observations that smaller-scale vorticity better aligns with the largest eigenvalue of larger-scale strain rate (Leung et al. 2012, Fiscaletti et al. 2016). Thus, while filtered

velocity gradient dynamics at a given scale ℓ lead to relatively inefficient alignments, smaller-scale velocity gradients align with larger-scale strain rate much more efficiently for energy transfer.

3.6. Lagrangian Nature of the Cascade

The energy cascade at scale ℓ occurs in the context of a flow with stronger larger-scale motions that sweep smaller-scale features (Drivas et al. 2017). This Lagrangian nature of the cascade was demonstrated by Wan et al. (2010), who computed the correlation coefficient of the energy dissipation rate with the energy cascade rate at an earlier time along a Lagrangian trajectory. Their key result demonstrated that the correlation peaks for a finite time lag $\Delta t_{\rm max} \sim \ell^{2/3}$, in agreement with K41 scaling, if the correlation is calculated along Lagrangian trajectories, whereas the equivalent Eulerian time correlation showed monotonic decay with increasing time lag. This finding complemented a study by Meneveau & Lund (1994), who demonstrated a similar Lagrangian correlation effect for scalewise kinetic energies.

The Lagrangian nature of the cascade was further highlighted by Ballouz et al. (2020). Building on the insight obtained by Ni et al. (2014) that vorticity alignment improves with cumulative Lagrangian strain over a finite time (the Cauchy-Green tensor), these authors showed that the efficiency of the cascade improves when considered in a fully Lagrangian way (using the Piola-Kirchoff stress tensor). In particular, they found that the efficiency for Π^{ℓ} calculated in this way peaks for a time interval that scales with K41 scaling, $\Delta t_{\rm max} \sim \ell^{2/3}$.

3.7. Irreversibility of the Cascade

Cascade dynamics at intermediate scales are assumed to be independent of viscosity, and the Euler equations are formally time reversible. Nonetheless, inertial dynamics can establish irreversibility in the statistical sense, even in the absence of viscosity (see section 3.1.3 of Davidson 2015). Vela-Martín & Jiménez (2021) numerically established an inverse energy cascade (from small to large scales) via specialized initial conditions, namely, reversing a velocity field obtained from decaying isotropic turbulence while using a time-reversible stress model. Averaging over an ensemble of simulations, they showed that the specialized initial condition can lead to a sustained inverse energy cascade, associated with vortex compression and strain-rate self-attenuation, revealing a mirrored teardrop shape in the QR PDF (Figure 6). However, with any slight perturbation from the specialized initial conditions, the dynamics quickly diverged from the inverse cascade to reestablish a forward cascade with strain self-amplification and vortex stretching. The results showed that the transition from inverse to forward cascade occurred simultaneously with the change in asymmetry of the QR PDF to the standard teardrop orientation (**Figure 6**). The

Piola-Kirchoff stress: a representation of the force per unit area according to a

reference state, back in time along a Lagrangian path

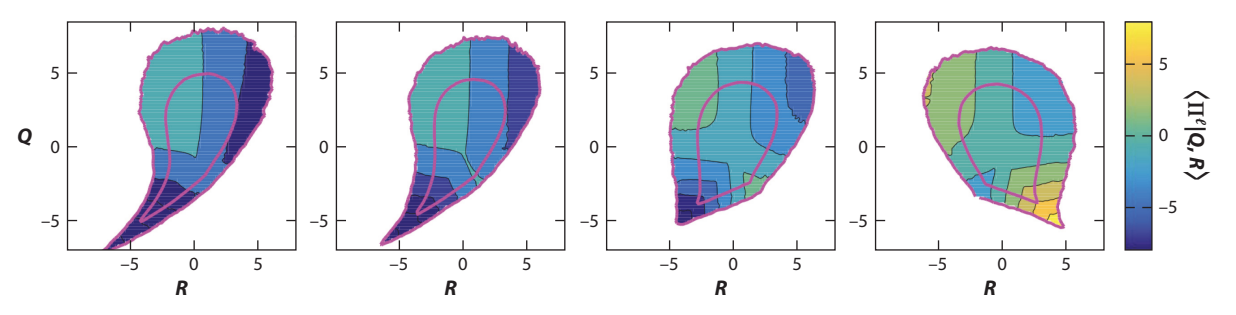


Figure 6

Isocontours of the OR probability density function from the filtered velocity gradient for four sequential times with perturbed time-reversed initial conditions. The QR space is colored at each time by the conditionally averaged cascade rate, $\langle \Pi^{\ell} | Q, R \rangle$. Figure adapted with permission from Vela-Martín & Jiménez (2021) (CC BY 4.0).

Dynamic model:

in the context of LES, a residual stress model for which the coefficients for an assumed model form are determined from the resolved velocity field asymmetry is most noticeable in the lower half of the *QR* plane, where the strain rate is dominant. These results are strong evidence that the direction of the energy cascade is set not by viscous dissipation but rather by inertial dynamics, predominantly strain-rate self-amplification. Viscosity allows for a stationary energy cascade by removing energy (preventing equipartition).

3.8. Implications for Large-Eddy Simulation Modeling

LES requires an approximation for τ_{ij}^{ℓ} , typically as a function of the local resolved VGT, $\overline{\mathbf{A}}^{\ell}$. Eddy viscosity models are common in practice (Meneveau & Katz 2000, Moser et al. 2021), but they assume instantaneous alignment between the strain-rate and residual stress eigenvectors as well as proportionality of their eigenvalues. The low cascade efficiency reported by Ballouz & Ouellette (2018) contradicts this assumption and concisely demonstrates the physical flaws of an eddy viscosity model. However, the higher efficiencies of multiscale interactions (Π_{s2} and $\Pi_{\omega 2}$) shown by Johnson (2021) present physical evidence in support of a mixed model consisting of a nonlinear gradient component that exactly represents the single-scale stresses (Π_{s1} and $\Pi_{\omega 1}$) plus an eddy viscosity component that approximates stresses arising from multiscale interactions.

The dynamic procedure presented by Germano et al. (1991) and Lilly (1992) is a popular LES strategy for determining model coefficients using a test filter with width $\ell' > \ell$ together with the Germano (1992) identity via assumed scale similarity. The theory developed by Johnson (2020, 2021) for energy cascade analysis also offers an alternative dynamic model that can be used to find coefficients by pen and paper, avoiding the need for a test filter calculation (Johnson 2022).

Finally, Vela-Martín (2022) devised a clever optimization scheme to demonstrate that a modified stress tensor with almost zero backscatter (i.e., local events of $\Pi^{\ell} < 0$) can be formed with identical divergence as τ_{ij}^{ℓ} . Therefore, the filtered NSE is unchanged by the near elimination of backscatter, implying that the incorporation of backscatter is not a necessary feature of accurate LES models.

4. LAGRANGIAN VELOCITY GRADIENT MODELS

Equation 5 (and its multiscale generalization in Equation 16) constitutes an attractive starting point for modeling because one of the main dynamical effects, gradient self-amplification, appears in closed form. The pressure Hessian and viscous diffusion, however, represent unclosed terms which need modeling in this framework.

4.1. A Brief Summary of Velocity Gradient Modeling Prior to 2010

To establish the necessary background for a review of more recent progress, this section provides an abridged account of velocity gradient modeling in the years prior to Meneveau's (2011) review, which presents a more thorough treatment. The simplest approach, neglecting the nonlocal pressure Hessian and viscous term, gives the restricted Euler model, which results in a finite-time singularity (see Section 2.5) (Vieillefosse 1982, 1984; Cantwell 1992). To obtain nonsingular dynamics that compare quantitatively with turbulence data, modeling of the unclosed pressure and viscous terms is evidently unavoidable.

One of the most influential works in the early development of Lagrangian velocity gradient models (Chertkov et al. 1999) was not based on the unfiltered (viscous range) velocity gradient equation (Equation 5). Chertkov et al. (1999) as well as Naso & Pumir (2005) modeled the dispersion of a tetrad of Lagrangian trajectories from which a perceived coarse-grained VGT can be inferred, providing insights into the multiscale gradient structure of turbulence.

Many other studies focused more explicitly on modeling the gradient of the NSE via Equation 5. Martín et al. (1998) attempted a linear damping model for the viscous Laplacian

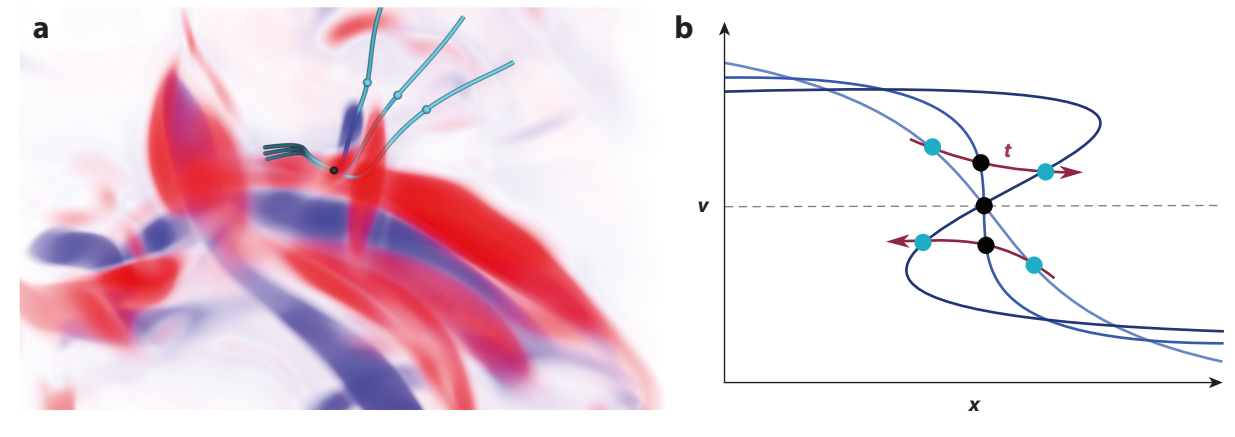


Figure 7

(a) Visualization of a sling event in a turbulent flow. The red and blue volume rendering shows the Q field (see **Figure 2**). The middle trajectory was taken from a direct numerical simulation, whereas the two accompanying trajectories were obtained by solving the linearized particle dynamics around that trajectory. (b) A sling event corresponds to the crossing of trajectories, which corresponds to a caustic in the particle velocity field v(x, t) not unlike a Burgers shock (see Equations 1 and 3). Figure provided by Tobias Bätge (see also Bätge et al. 2023).

and neglected the nonlocal pressure Hessian, but it proved insufficient for regularizing the finite-time singularity for larger gradients. Interestingly, this analysis provides some insight into the behavior of inertial particles in turbulence, where finite-time singularities correspond to caustics in the particle velocity field (**Figure 7**) (see the sidebar titled Velocity Gradients in Particle-Laden Turbulence). Nonetheless, for models of the fluid VGT, nonlinear relaxation is needed. To this end, Jeong & Girimaji (2003) introduced the use of the Cauchy–Green tensor to encode Lagrangian deformation in the closure of the viscous term, successfully regularizing the finite-time singularity while still entirely neglecting the nonlocal pressure Hessian.

Chevillard & Meneveau (2006) developed the recent fluid deformation (RFD) model, which uses a short-time approximation of the Cauchy–Green tensor to approximate both the viscous Laplacian and the nonlocal pressure Hessian in a consistent manner. The RFD model also features an additive stochastic forcing which takes into account the forcing of the flow along with fluctuations not contained in the deterministic closure. The resulting model equations take the nondimensional form

$$dA_{ij} = \begin{bmatrix} -A_{ik}A_{kj} + \underbrace{C_{ij}^{-1}}_{\text{pressure Hessian}} A_{lm}A_{ml} - \underbrace{\frac{1}{3}C_{kk}^{-1}A_{ij}}_{\text{viscous damping}} \end{bmatrix} dt + dF_{ij},$$
 21.

where dF_{ij} is the increment of a tensorial Wiener process featuring a covariance that complies with incompressibility, homogeneity, and isotropy (Chevillard et al. 2008). The pressure Hessian model bears the marks of inspiration from the tetrad model of Chertkov et al. (1999), with the Cauchy–Green tensor taking the place of the tetrad's moment of inertia tensor. The viscous model resembles that of Jeong & Girimaji (2003). In RFD, however, the Cauchy–Green tensor is evaluated at a fixed short time, so that Equation 21 constitutes a closed stochastic model for the evolution of velocity gradients along Lagrangian trajectories. Chevillard & Meneveau (2011) showed that the RFD model qualitatively captures the pirouette effect of Xu et al. (2011). **Figure 8** depicts the *QR* PDF from the RFD model along with a comparison to DNS data and

Wiener process:

a continuous, Gaussian stochastic process with zero mean, a variance equal to time, and independent increments

VELOCITY GRADIENTS IN PARTICLE-LADEN TURBULENCE

Velocity gradients play an important role in particle-laden turbulent flows, causing (heavy) particles to preferentially concentrate in flow regions where Q is negative (Maxey 1987, Eaton & Fessler 1994, Esmaily-Moghadam & Mani 2016), which can dramatically affect particle collision rates (Sundaram & Collins 1997). Enhanced collision rates are facilitated by the so-called sling effect, which can generate trajectory crossings, or caustics (Falkovich et al. 2002, Wilkinson & Mehlig 2005, Bewley et al. 2013) (**Figure 7**). Using the Stokes drag law for the particle velocity v_i , $dv_i/dt = (u_i - v_i)/\tau_p$, where τ_p is the particle relaxation timescale and u_i is the fluid velocity encountered by the particle, one can describe the relative motion of nearby particles by using a particle velocity gradient, $P_{ij} = \partial v_i/\partial x_j$. Along particle trajectories,

$$\frac{\mathrm{d}P_{ij}}{\mathrm{d}t} = \frac{A_{ij} - P_{ij}}{\tau_{\mathrm{p}}} - P_{ik}P_{kj}.$$
 SB5.

Here, A_{ij} is the fluid VGT evaluated at the particle location. The particle VGT relaxes toward the fluid VGT but is also subject to gradient self-amplification. It is known from the VGT modeling literature (Martín et al. 1998) that linear relaxation removes finite-time singularities only for relatively small values of the VGT. Thus, finite-time singularities of the particle VGT corresponding to caustic formation are not averted by Stokes drag. Johnson & Meneveau (2017a) extended the restricted Euler model to the fluid VGT dynamics along inertial particle trajectories.

Meibohm et al. (2023) recently used a fixed-point analysis to derive a characteristic threshold in *QR*-invariant space that marks the onset of a sling event using the fluid VGT. Independently, Bätge et al. (2023) derived a simple criterion for predicting caustics, which showed evidence that trajectory crossing events are controlled by the most negative eigenvalue of the fluid VGT. Bec et al. (2024) present a broader review of the topic in this volume.

other models discussed below. While it captures the asymmetric teardrop shape, quantitative differences compared to the *QR* PDF from DNS are apparent. Recently, Apolinário et al. (2019) further investigated the statistical properties of the RFD model using field-theoretic methods.

Equation 21 illustrates how stochastic differential equations naturally occur in the context of velocity gradient modeling. In fact, the connection between stochastic modeling of Lagrangian velocity gradients and PDF methods had already been established by Girimaji & Pope (1990). They derived a Fokker–Planck equation for the PDF of velocity gradients and proposed a closure model that imposes constraints on the moments to yield log-normal dissipation statistics.

4.2. Recent Developments in Velocity Gradient Modeling

More recently, using PDF methods (Pope 2000), Wilczek & Meneveau (2014) considered the exact Fokker–Planck equation for the velocity gradient statistics of a stochastically forced NSE, which takes the form

$$\frac{\partial}{\partial t} f(\mathbf{A}; t) = -\frac{\partial}{\partial \mathcal{A}_{ij}} \left(\left[-\left(\mathcal{A}_{ik} \mathcal{A}_{kj} - \frac{1}{3} \operatorname{Tr} \left(\mathbf{A}^2 \right) \delta_{ij} \right) - \left\langle \widetilde{H}_{ij} \middle| \mathbf{A} \right\rangle + \left\langle \nu \nabla^2 A_{ij} \middle| \mathbf{A} \right\rangle \right] f(\mathbf{A}; t) \right)
+ \frac{1}{2} Q_{ijkl}(\mathbf{0}) \frac{\partial}{\partial \mathcal{A}_{ik}} \frac{\partial}{\partial \mathcal{A}_{ij}} f(\mathbf{A}; t).$$
22.

Here, f(A; t) denotes the single-point, single-time PDF of the velocity gradient with the sample-space variable A. The drift term in this Fokker–Planck equation consists of the restricted Euler term (see Equation 13), which appears in closed form, and two unclosed terms. The unclosed

Fokker-Planck equation:

a partial differential equation for the evolution of the PDF in sample space for a stochastic process described by a Langevin equation

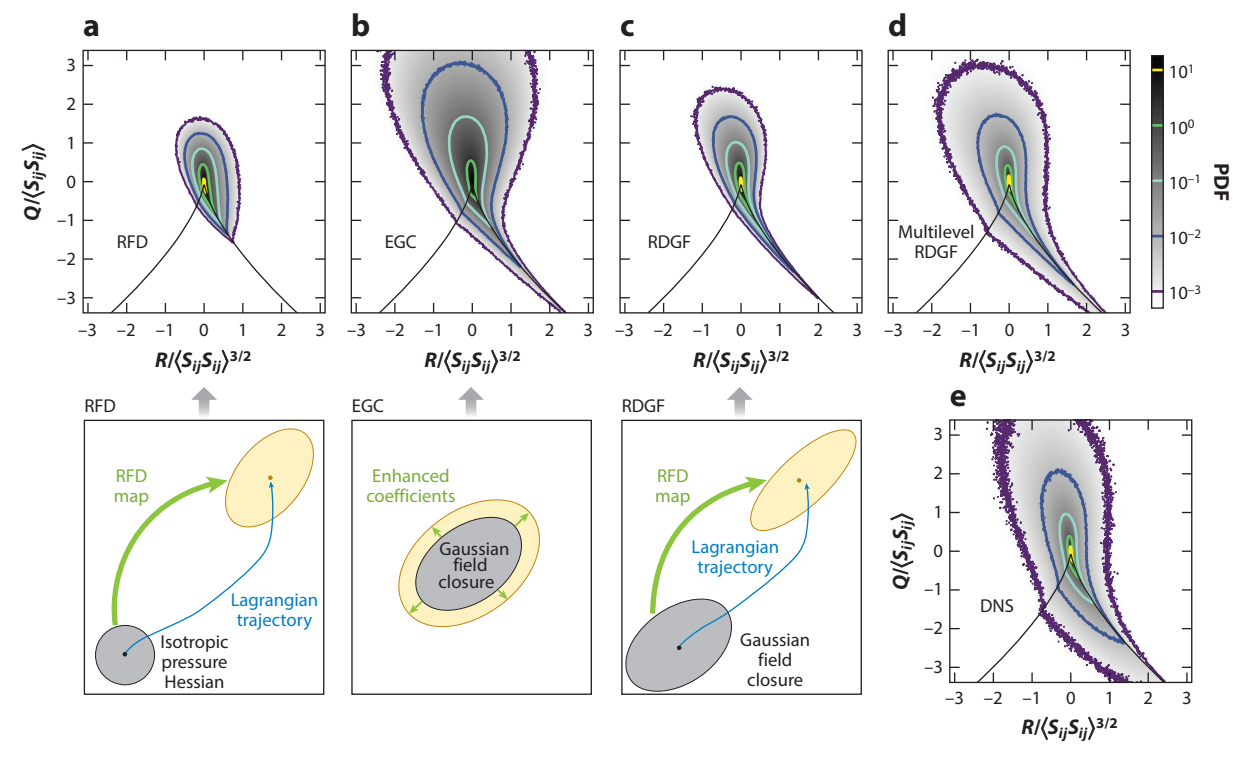


Figure 8

Comparison of the *QR* probability density function from various velocity gradient models and direct numerical simulations (DNS). (a) Recent fluid deformation (RFD) model (Chevillard & Meneveau 2006). (b) Enhanced Gaussian closure (EGC) model (Wilczek & Meneveau 2014). (c) Recent fluid deformation from Gaussian fields (RDGF) model (Johnson & Meneveau 2016a). (d) Multiscale model (Johnson & Meneveau 2017b). (e) DNS (Li et al. 2008).

terms take the form of conditional averages involving information not contained in a single-point description; $\langle \widetilde{H}_{ij} | \mathcal{A} \rangle$ is the conditional mean nonlocal pressure Hessian given a velocity gradient \mathcal{A} , and $\langle \nu \nabla^2 A_{ij} | \mathcal{A} \rangle$ is the conditional mean viscous Laplacian of the velocity gradient. The diffusion term depends on the covariance of the stochastic force, \mathbf{Q} .

The Fokker–Planck equation for the velocity gradient PDF corresponds to the Langevin equation (Wilczek & Meneveau 2014)

$$d\mathcal{A}_{ij} = \left[-\left(\mathcal{A}_{ik} \mathcal{A}_{kj} - \frac{1}{3} \operatorname{Tr} \left(\mathcal{A}^2 \right) \delta_{ij} \right) - \left\langle \widetilde{H}_{ij} \middle| \mathcal{A} \right\rangle + \left\langle \nu \nabla^2 A_{ij} \middle| \mathcal{A} \right\rangle \right] dt + dF_{ij},$$
 23.

whose realizations match the VGT single-time statistics. This equation is conceptually very similar to the phenomenologically derived Langevin equation of the RFD model (Equation 21), which aims to directly model the VGT evolution along individual Lagrangian trajectories. In this sense, Equation 23 highlights the connection between the inherently statistical approach from Girimaji & Pope (1990) with physics-based modeling from RFD and its precursors.

Using the statistical framework of the Lundgren (1967)–Monin (1967)–Novikov (1967) hierarchy (for a review, see, e.g., Friedrich et al. 2012), the nonlocal information contained in these terms can be made explicit in terms of two-point statistics of the velocity gradient field. As a closure approximation, Wilczek & Meneveau (2014) evaluated the conditional averages for isotropic Gaussian velocity fields, which are fully characterized by the energy spectrum. The viscous term

Langevin equation: a stochastic differential equation describing the evolution of a single realization of a stochastic process

result is

Gaussian field:

a random field in which the joint statistics of the field values at any combination of *N* points are joint normal

$$\langle \nu \nabla^2 \mathbf{A} | \mathbf{A} \rangle = \delta \mathbf{A}, \quad \text{with} \quad \delta = -\nu \frac{\int dk \, k^4 \, E(k)}{\int dk \, k^2 \, E(k)}.$$
 24.

This result resembles the linear diffusion model of Martín et al. (1998); δ is an inverse timescale determined by the energy spectrum, E(k). For the nonlocal pressure Hessian, the Gaussian closure yields

$$\langle \widetilde{\mathbf{H}} | \mathcal{A} \rangle = \alpha \left[\mathcal{S}^2 - \frac{\mathbf{I}}{3} \operatorname{Tr} \left(\mathcal{S}^2 \right) \right] + \beta \left[\mathcal{W}^2 - \frac{\mathbf{I}}{3} \operatorname{Tr} \left(\mathcal{W}^2 \right) \right] + \gamma \left(\mathcal{S} \mathcal{W} - \mathcal{W} \mathcal{S} \right).$$
 25.

Here **I** is the identity tensor, and \mathcal{S} and \mathcal{W} denote the sample-space variables for the strain-rate and rotation-rate tensors, respectively. The coefficients $\alpha = -2/7$ and $\beta = -2/5$ are independent of the energy spectrum of the Gaussian fields, whereas γ depends on the energy spectrum.

Wilczek & Meneveau (2014) observed that the Gaussian field closure for the conditional Laplacian term (Equation 24) and the conditional pressure Hessian term (Equation 25) is not sufficient to regularize the modeled velocity gradient dynamics. To mitigate this problem, they proposed the enhanced Gaussian closure (EGC) model, in which the structure of the tensorial terms is maintained but the coefficients of the model terms are estimated from DNS data. The estimated values of α and β from DNS were larger in magnitude than those of the Gaussian calculation. Use of the EGC model prevented singularity and led to stationary statistics.

Figure 8 illustrates the QR PDF from the EGC model. Compared with the RFD model, this model generates much larger velocity gradients. In comparison to DNS data, though, it is evident that the frequency of vorticity-dominated events (Q>0) is overemphasized, highlighting the conceptual difficulty of enforcing global constraints such as the Betchov (1956) relations when modeling at a single-point or single-particle level. Similar to Girimaji & Pope (1990), Johnson & Meneveau (2016a) as well as Leppin & Wilczek (2020) demonstrated that such constraints can be imposed at the level of an ensemble of stochastic trajectories and used to reduce the number of free parameters in the model.

In their recent fluid deformation from Gaussian fields (RDGF) closure, Johnson & Meneveau (2016a) combined the RFD closure model with the Gaussian field closure by assuming initially Gaussian fields that are then subject to recent fluid deformation as modeled by the RFD mapping. For example, the pressure Hessian closure becomes

$$\langle H_{ij} | \mathbf{A} \rangle = -\frac{C_{ij}^{-1}}{C_{ii}^{-1}} \operatorname{Tr} \left(\mathbf{A}^2 \right) + G_{ij} - \frac{C_{ij}^{-1}}{C_{ii}^{-1}} \operatorname{Tr} \left(\mathbf{G} \right),$$
 26.

where G is the nonlocal Gaussian pressure Hessian closure (Equation 25), subject to recent deformation mapping. In this way, anisotropic pressure Hessian contributions previously neglected in the RFD closure can be naturally included. If the Cauchy–Green tensor is taken as the identity tensor in RDGF (corresponding to removal of the deformation mapping), then the Gaussian field closure is recovered. Alternatively, if the nonlocal Gaussian pressure Hessian is removed, G = 0, then RDGF simplifies to the RFD model. The RDGF model thus leverages the strengths of both previous models to incorporate both nonlocal pressure information and Lagrangian history effects while avoiding the need to adjust the Gaussian field coefficients using DNS. The resulting RDGF model shows improved quantitative agreement with DNS for various velocity gradient statistics such as PDFs of velocity gradient components, the *QR* PDF (**Figure 8**), and alignment statistics between the vorticity and the principal axes of strain.

A major drawback of the recent models discussed above is that they cannot account for the increase in active spatiotemporal scales and intermittency with Reynolds number in a robust

manner (e.g., Martins Afonso & Meneveau 2010). Biferale et al. (2007) made the first attempt to address this issue by building a multiscale velocity gradient shell model. More recently, Johnson & Meneveau (2017b) generalized the RDGF to a hierarchical model featuring multiple timescales. This model draws on the structure of the filtered velocity gradient dynamics (Equation 16) and considers the action of filtered, larger-scale velocity gradients on smaller-scale velocity gradients by imposing a local timescale determined by the larger scales, $\tau_n(t)$, such that

$$d\overline{A}_{ij}^{(n)} = \left[-\left(\overline{A}_{ik}^{(n)}\overline{A}_{kj}^{(n)} - \frac{1}{3}\overline{A}_{lm}^{(n)}\overline{A}_{ml}^{(n)}\delta_{ij}\right) - \frac{1}{\tau_n}\frac{d\tau_n}{dt}\overline{A}_{ij}^{(n)} + h_{ij}^{(n)}(\overline{\mathbf{A}}^{(n)}, \tau_n)\right]dt + dF_{ij}^{(n)},$$
 27.

where $\overline{A}_{ij}^{(n)}$ is the velocity gradient filtered at the *n*th level and $b_{ij}^{(n)}$ represents a closure model for the pressure Hessian, viscous Laplacian, and residual stress terms. Increasing the Reynolds number corresponds to including additional velocity gradient levels representing successively smaller scales. The modulation of the timescales by larger-scale motion leads to more rapid and intense fluctuations of the smaller-scale gradients, accurately reproducing intermittency scaling of phenomenological cascade models such as the *p* model (Meneveau & Sreenivasan 1987), the log-normal model (Oboukhov 1962, Kolmogorov 1962), and the She–Lévêque model (She & Lévêque 1994). Meanwhile, the velocity gradient statistics at any given Reynolds number produced improved realism (e.g., as shown for the *QR* PDF in **Figure 8**). Luo et al. (2022) showed that the multiscale RDGF model can be simplified using convolution techniques. Independently, Pereira et al. (2018) built on the approach of Girimaji & Pope (1990) to construct a model constrained to match desired multifractal statistics with realistic Reynolds number trends.

Johnson & Meneveau (2018) used the timescale coupling of Johnson & Meneveau (2017b) as a basis for coupling Lagrangian velocity gradients with LES to enrich the filtered field with small-scale dynamics. By coupling the RDGF model to resolved velocity gradients from channel flow LES, excellent agreement with velocity gradient statistics from fully resolved DNS was achieved at a fraction of the cost. Johnson & Meneveau (2018) also highlighted the possibility of using this approach to model unresolved droplet deformation in LES.

4.3. Insights from Experiments and Direct Numerical Simulations for Modeling

Experiments and DNS provide important insights to inform models. For example, Lawson & Dawson (2015) obtained the conditionally averaged field of the second invariant Q from a von Kármán swirling-flow experiment using particle image velocimetry (Lawson & Dawson 2014) as well as from DNS data (Li et al. 2008). Their results showed how well-known features of turbulent fields (e.g., the fact that intense vorticity is accompanied by neighboring regions of strain; Figure 2) translate into conditional Q statistics, which are necessary to close the nonlocal pressure Hessian in Equation 22 (see also Equation 12). They also highlighted the connection between the EGC and stochastic estimation (e.g., Adrian 1994). Additionally, Lawson & Dawson (2015) obtained interesting alignment statistics of the pressure Hessian, which may be used as a benchmark for velocity gradient models. Carbone et al. (2020) studied the velocity gradient dynamics in the strain eigenframe, thereby revealing an interesting symmetry reduction property of the pressure Hessian that might be useful for improving pressure Hessian models. Leppin & Wilczek (2020) made a similar observation, showing that the γ term in Equation 25 leaves the single-time statistics invariant and can be used to tune the time correlations of the velocity gradient model. Das & Girimaji (2019) showed that, compared with the full VGT, the VGT normalized by its magnitude varies little with Reynolds number. On this basis, Das & Girimaji (2023) modeled the normalized VGT separately from the VGT magnitude. Recent conditional enstrophy, dissipation, and pressure Hessian statistics from DNS at high–Reynolds number turbulence (Buaria et al. 2020a, 2022; Buaria & Pumir 2023) offer additional reference points for future improvements of velocity gradient models.

4.4. Data-Driven Modeling

As in many areas of fluid dynamics, machine learning has spurred new developments in modeling the unclosed terms for Lagrangian velocity gradient evolution. Since the nonlocal pressure Hessian is traceless and symmetric, it shares formal similarities with the deviatoric part of the Reynolds stress tensor needed for Reynolds-averaged Navier–Stokes (RANS) modeling. In the RANS context, Ling et al. (2016) proposed a machine learning framework using so-called tensor-based neural networks (TBNNs), which built the essential invariance properties into the network design. Various researchers have adapted this approach to Lagrangian velocity gradient modeling. Using a TBNN approach, Parashar et al. (2020) demonstrated improved pressure Hessian modeling compared with the RFD model. Tian et al. (2021) used the TBNN approach to build a stochastic Lagrangian model that exhibits improvements over previous modeling approaches. Furthermore, they successfully extended the approach to the modeling of coarse-grained velocity gradients. The latest results by Buaria & Sreenivasan (2023) show that such approaches could even be used to predict velocity gradient statistics at Reynolds numbers that exceed those of the training data sets.

SUMMARY POINTS

- 1. Investigations of fundamental turbulence physics at small and intermediate scales have seen significant progress in recent years through the study of velocity gradient statistics, dynamics, and structure.
- 2. The dual challenge of nonlinearity and nonlocality in turbulence has long flum-moxed theoreticians and modelers alike. A Lagrangian perspective on velocity gradients efficiently expresses the nonlinearity of Navier–Stokes dynamics as gradient self-amplification, and recent research has leveraged this framework to build a deeper understanding of nonlocality such as pressure effects.
- 3. The energy cascade has long been understood qualitatively in terms of multiscale interactions between rotational and straining fluid motions. Recent theoretical innovations and continued advances in direct numerical simulations (DNS) have placed this understanding on a firm quantitative footing while illuminating the importance of strain-rate self-amplification, with implications for large-eddy simulation (LES) models.
- 4. Lagrangian velocity gradient models naturally incorporate nonlinear effects at low cost, and their ability to accurately represent the (unclosed) multiscale and nonlocal effects of turbulence has significantly improved. In addition to vital theoretical tools for understanding fundamental turbulence physics, Lagrangian velocity gradient models have shown some evidence of practical applicability for predicting particle-laden and multiphase flows.
- 5. Multiscale velocity gradients have provided a common mathematical framework for theory and modeling efforts to interact seamlessly. This confluence promises further progress in years to come, both on the fundamental side and with respect to applications.

FUTURE ISSUES

- The incorporation of fundamental advances in nonlocal physics into (affordable)
 Lagrangian velocity gradient closure models is very much a work in progress. Remaining
 challenges include generation of more accurate conditional and multipoint/multitime
 statistics, increased realism of multiscale interactions, quantitative prediction of intermittency at high Reynolds numbers, and increased fidelity for particle-laden flows.
- 2. Machine learning has emerged as a potentially powerful tool that could accelerate future advances in Lagrangian modeling. The low dimensionality, nonlinear dynamics, and non-Gaussian statistics of velocity gradients promise to be beneficial for understanding turbulence physics and machine learning algorithm development alike.
- 3. Further development in the hybridization of (multiscale) Lagrangian velocity gradient models with LES could open up new areas of application.
- 4. Multiscale velocity gradients have proven to be a valuable framework for a unified statistical, dynamical, and structural understanding of classical turbulence theory, focusing mostly on the flow regime corresponding to Kolmogorov's similarity hypotheses. Given the practical importance of more complex flow regimes, such as near-wall or multiphase turbulence, innovative extensions of this framework could have a far-reaching impact on the study and prediction of turbulent flows.

DISCLOSURE STATEMENT

The authors are not aware of any biases that might be perceived as affecting the objectivity of this review.

ACKNOWLEDGMENTS

The authors gratefully acknowledge assistance from Cristian C. Lalescu for preparing Figure 2, Lukas Bentkamp for preparing Figure 5, and Tobias Bätge for preparing Figure 7. Gabriel B. Apolinário, Lukas Bentkamp, Andy Bragg, Dhawal Buaria, Maurizio Carbone, Itzhak Fouxon, John Lawson, Charles Meneveau, Alain Pumir, and Alberto Vela-Martín provided helpful reviews of a draft of this article. This material is based on research supported by the National Science Foundation under grant 2152373. This article is part of a project that has received funding from the European Research Council under the European Union's Horizon 2020 research and innovation program (grant agreement number 101001081). The authors gratefully acknowledge the Gauss Centre for Supercomputing e.V. (GCS; https://www.gauss-centre.eu) for funding this project by providing computing time on the GCS Supercomputer SuperMUC-NG at Leibniz Supercomputing Centre (https://www.lrz.de). Computational resources provided by the Max Planck Computing and Data Facility are also gratefully acknowledged.

LITERATURE CITED

Adrian RJ. 1994. Stochastic estimation of conditional structure: a review. Appl. Sci. Res. 53:291–303Apolinário GB, Moriconi L, Pereira RM. 2019. Instantons and fluctuations in a Lagrangian model of turbulence. Physica A 514:741–57

Ashurst WT, Kerstein AR, Kerr RM, Gibson CH. 1987. Alignment of vorticity and scalar gradient with strain rate in simulated Navier–Stokes turbulence. *Phys. Fluids* 30(8):2343–53

- Ballouz JG, Johnson PL, Ouellette NT. 2020. Temporal dynamics of the alignment of the turbulent stress and strain rate. *Phys. Rev. Fluids* 5:114606
- Ballouz JG, Ouellette NT. 2018. Tensor geometry in the turbulent cascade. J. Fluid Mech. 835:1048-64
- Bätge T, Fouxon I, Wilczek M. 2023. Quantitative prediction of sling events in turbulence at high Reynolds numbers. *Phys. Rev. Lett.* 131:054001
- Bec J, Gustavsson K, Mehlig B. 2024. Statistical models for the dynamics of heavy particles in turbulence. Annu. Rev. Fluid Mech. 56:189–213
- Bec J, Khanin K. 2007. Burgers turbulence. Phys. Rep. 447(1/2):1-66
- Betchov R. 1956. An inequality concerning the production of vorticity in isotropic turbulence. *J. Fluid Mech.* 1(5):497–504
- Bewley GP, Saw EW, Bodenschatz E. 2013. Observation of the sling effect. New J. Phys. 15:083051
- Biferale L, Chevillard L, Meneveau C, Toschi F. 2007. Multiscale model of gradient evolution in turbulent flows. *Phys. Rev. Lett.* 98:214501
- Borue V, Orszag SA. 1998. Local energy flux and subgrid-scale statistics in three-dimensional turbulence. 7. Fluid Mech. 366:1–31
- Buaria D, Bodenschatz E, Pumir A. 2020a. Vortex stretching and enstrophy production in high Reynolds number turbulence. *Phys. Rev. Fluids* 5:104602
- Buaria D, Pumir A. 2021. Nonlocal amplification of intense vorticity in turbulent flows. Phys. Rev. Res. 3:L042020
- Buaria D, Pumir A. 2022. Vorticity–strain rate dynamics and the smallest scales of turbulence. Phys. Rev. Lett. 128:094501
- Buaria D, Pumir A. 2023. Role of pressure in the dynamics of intense velocity gradients in turbulent flows. 7. Fluid Mecb. 973:A23
- Buaria D, Pumir A, Bodenschatz E. 2020b. Self-attenuation of extreme events in Navier–Stokes turbulence. Nat. Commun. 11:5852
- Buaria D, Pumir A, Bodenschatz E. 2022. Generation of intense dissipation in high Reynolds number turbulence. *Philos. Trans. R. Soc. A* 380(2218):20210088
- Buaria D, Pumir A, Bodenschatz E, Yeung PK. 2019. Extreme velocity gradients in turbulent flows. New J. Phys. 21:043004
- Buaria D, Sreenivasan KR. 2020. Dissipation range of the energy spectrum in high Reynolds number turbulence. *Phys. Rev. Fluids* 5:092601
- Buaria D, Sreenivasan KR. 2023. Forecasting small scale dynamics of fluid turbulence using deep neural networks. PNAS 120(30):e2305765120
- Bürger K, Treib M, Westermann R, Werner S, Lalescu CC, et al. 2012. Vortices within vortices: hierarchical nature of vortex tubes in turbulence. arXiv:1210.3325 [physics.flu-dyn]
- Burgers JM. 1948. A mathematical model illustrating the theory of turbulence. Adv. Appl. Mech. 1:171-99
- Cantwell BJ. 1992. Exact solution of a restricted Euler equation for the velocity gradient tensor. *Phys. Fluids* 4(4):782–93
- Carbone M, Bragg AD. 2020. Is vortex stretching the main cause of the turbulent energy cascade? *J. Fluid Mech.* 883:R2
- Carbone M, Iovieno M, Bragg AD. 2020. Symmetry transformation and dimensionality reduction of the anisotropic pressure Hessian. 7. Fluid Mech. 900:A38
- Carbone M, Wilczek M. 2022. Only two Betchov homogeneity constraints exist for isotropic turbulence. 7. Fluid Mecb. 948:R2
- Chertkov M, Pumir A, Shraiman B. 1999. Lagrangian tetrad dynamics and the phenomenology of turbulence. Phys. Fluids 11(8):2394–410
- Chevillard L, Meneveau C. 2006. Lagrangian dynamics and statistical geometric structure of turbulence. Phys. Rev. Lett. 97:174501
- Chevillard L, Meneveau C. 2011. Lagrangian time correlations of vorticity alignments in isotropic turbulence: observations and model predictions. *Phys. Fluids* 23:101704
- Chevillard L, Meneveau C, Biferale L, Toschi F. 2008. Modeling the pressure Hessian and viscous Laplacian in turbulence: comparisons with direct numerical simulation and implications on velocity gradient dynamics. *Phys. Fluids* 20:101504

- Clark RA, Ferziger JH, Reynolds WC. 1979. Evaluation of subgrid-scale models using an accurately simulated turbulent flow. 7. Fluid Mech. 91(1):1–16
- Constantin P, Iyer G. 2008. A stochastic Lagrangian representation of the three-dimensional incompressible Navier–Stokes equations. Commun. Pure Appl. Math. 61(3):330–45
- Danish M, Meneveau C. 2018. Multiscale analysis of the invariants of the velocity gradient tensor in isotropic turbulence. Phys. Rev. Fluids 3:044604
- Das R, Girimaji SS. 2019. On the Reynolds number dependence of velocity-gradient structure and dynamics. 7. Fluid Mech. 861:163–79
- Das R, Girimaji SS. 2020. Revisiting turbulence small-scale behavior using velocity gradient triple decomposition. New J. Phys. 22:063015
- Das R, Girimaji SS. 2023. Data-driven model for Lagrangian evolution of velocity gradients in incompressible turbulent flows. arXiv:2304.14529 [physics.flu-dyn]
- Davidson PA. 2011. Long-range interactions in turbulence and the energy decay problem. *Philos. Trans. R. Soc.* A 369(1937):796–810
- Davidson PA. 2015. Turbulence: An Introduction for Scientists and Engineers. Oxford, UK: Oxford Univ. Press
- de Kármán T, Howarth L. 1938. On the statistical theory of isotropic turbulence. *Proc. R. Soc. A* 164(917):192–215
- Doan NAK, Swaminathan N, Davidson PA, Tanahashi M. 2018. Scale locality of the energy cascade using real space quantities. Phys. Rev. Fluids 3:084601
- Douady S, Couder Y, Brachet ME. 1991. Direct observation of the intermittency of intense vorticity filaments in turbulence. *Phys. Rev. Lett.* 67:983–86
- Drivas TD, Johnson PL, Lalescu CC, Wilczek M. 2017. Large-scale sweeping of small-scale eddies in turbulence: a filtering approach. Phys. Rev. Fluids 2:104603
- Dubrulle B. 2019. Beyond Kolmogorov cascades. J. Fluid Mech. 867:P1
- Eaton J, Fessler J. 1994. Preferential concentration of particles by turbulence. Int. J. Multipb. Flow 20:169-209
- Esmaily-Moghadam M, Mani A. 2016. Analysis of the clustering of inertial particles in turbulent flows. *Phys. Rev. Fluids* 1:084202
- Eyink GL. 1995. Local energy flux and the refined similarity hypothesis. J. Stat. Phys. 78(1/2):335-51
- Eyink GL. 2006. Multi-scale gradient expansion of the turbulent stress tensor. 7. Fluid Mech. 549:159-90
- Eyink GL. 2007. Turbulence theory. Course Not., Johns Hopkins Univ., Baltimore, MD. https://www.ams.jhu.edu/~eyink/Turbulence/notes.html
- Eyink GL, Sreenivasan KR. 2006. Onsager and the theory of hydrodynamic turbulence. *Rev. Mod. Phys.* 78(1):87–135
- Falkovich G, Fouxon A, Stepanov MG. 2002. Acceleration of rain initiation by cloud turbulence. Nature 419(6903):151–54
- Fiscaletti D, Elsinga GE, Attili A, Bisetti F, Buxton ORH. 2016. Scale dependence of the alignment between strain rate and rotation in turbulent shear flow. *Phys. Rev. Fluids* 1:064405
- Friedrich R, Daitche A, Kamps O, Lülff J, Voßkuhle M, Wilczek M. 2012. The Lundgren–Monin–Novikov hierarchy: kinetic equations for turbulence. C. R. Phys. 13(9/10):929–53
- Frisch U. 1995. Turbulence: The Legacy of A.N. Kolmogorov. Cambridge, UK: Cambridge Univ. Press
- Frisch U, Bec J. 2002. Burgulence. In New Trends in Turbulence. Turbulence: Nouveaux Aspects. Les Houches Session LXXIV, 31 July–1 September 2000, pp. 341–83. Berlin: Springer
- Gao Y, Liu C. 2019. Rortex based velocity gradient tensor decomposition. Phys. Fluids 31:011704
- Germano M. 1992. Turbulence: the filtering approach. 7. Fluid Mech. 238:325–36
- Germano M, Piomelli U, Moin P, Cabot WH. 1991. A dynamic subgrid-scale eddy viscosity model. *Phys. Fluids A* 3(7):1760–65
- Girimaji SS, Pope SB. 1990. A diffusion model for velocity gradients in turbulence. *Phys. Fluids A* 2(2):242–56 Gulitski G, Kholmyansky M, Kinzelbach W, Lüthi B, Tsinober A, Yorish S. 2007. Velocity and temperature
 - derivatives in high-Reynolds-number turbulent flows in the atmospheric surface layer. Part 1. Facilities, methods and some general results. *7. Fluid Mech.* 589:57–81
- Hamlington PE, Schumacher J, Dahm WJA. 2008. Local and nonlocal strain rate fields and vorticity alignment in turbulent flows. Phys. Rev. E 77:026303

- Hill RJ. 2001. Equations relating structure functions of all orders. J. Fluid Mech. 434:379-88
- Holzner M, Guala M, Lüthi B, Liberzon A, Nikitin N, et al. 2010. Viscous tilting and production of vorticity in homogeneous turbulence. *Phys. Fluids* 22:061701
- Ishihara T, Gotoh T, Kaneda Y. 2009. Study of high-Reynolds number isotropic turbulence by direct numerical simulation. Annu. Rev. Fluid Mech. 41:165–80
- Jeong E, Girimaji SS. 2003. Velocity-gradient dynamics in turbulence: effect of viscosity and forcing. Theor. Comput. Fluid. Dyn. 16(6):421–32
- Jiménez J, Wray AA, Saffman PG, Rogallo RS. 1993. The structure of intense vorticity in isotropic turbulence. J. Fluid Mecb. 255:65–90
- Johnson PL. 2020. Energy transfer from large to small scales in turbulence by multiscale nonlinear strain and vorticity interactions. Phys. Rev. Lett. 124:104501
- Johnson PL. 2021. On the role of vorticity stretching and strain self-amplification in the turbulence energy cascade. J. Fluid Mech. 922:A3
- Johnson PL. 2022. A physics-inspired alternative to spatial filtering for large-eddy simulations of turbulent flows. 7. Fluid Mech. 934:A30
- Johnson PL, Meneveau C. 2016a. A closure for Lagrangian velocity gradient evolution in turbulence using recent-deformation mapping of initially Gaussian fields. J. Fluid Mech. 804:387–419
- Johnson PL, Meneveau C. 2016b. Large-deviation statistics of vorticity stretching in isotropic turbulence. Phys. Rev. E 93:033118
- Johnson PL, Meneveau C. 2017a. Restricted Euler dynamics along trajectories of small inertial particles in turbulence. J. Fluid Mech. 816:R2
- Johnson PL, Meneveau C. 2017b. Turbulence intermittency in a multiple-time-scale Navier-Stokes-based reduced model. Phys. Rev. Fluids 2:072601(R)
- Johnson PL, Meneveau C. 2018. Predicting viscous-range velocity gradient dynamics in large-eddy simulations of turbulence. J. Fluid Mech. 837:80–114
- Keylock CJ. 2018. The Schur decomposition of the velocity gradient tensor for turbulent flows. J. Fluid Mech. 848:876–905
- Khurshid S, Donzis DA, Sreenivasan KR. 2018. Energy spectrum in the dissipation range. *Phys. Rev. Fluids* 3:082601(R)
- Kolmogorov AN. 1941a. Dissipation of energy in the locally isotropic turbulence. *Dokl. Akad. Nauk SSSR* 32:16–18 (in Russian); 1991. *Proc. R. Soc. A* 434:15–17 (English transl.)
- Kolmogorov AN. 1941b. The local structure of turbulence in incompressible viscous fluid for very large Reynolds numbers. *Dokl. Akad. Nauk SSSR* 30(4):301–5 (in Russian); 1991. *Proc. R. Soc. A* 434:9–13 (English transl.)
- Kolmogorov AN. 1962. A refinement of previous hypotheses concerning the local structure of turbulence in a viscous incompressible fluid at high Reynolds number. *J. Fluid Mech.* 13(1):82–85
- Lawson JM, Dawson JR. 2014. A scanning PIV method for fine-scale turbulence measurements. *Exp. Fluids* 55(12):1857
- Lawson JM, Dawson JR. 2015. On velocity gradient dynamics and turbulent structure. J. Fluid Mech. 780:60–98Leppin LA, Wilczek M. 2020. Capturing velocity gradients and particle rotation rates in turbulence. Phys. Rev. Lett. 125:224501
- Leung T, Swaminathan N, Davidson PA. 2012. Geometry and interaction of structures in homogeneous isotropic turbulence. *7. Fluid Mech.* 710:453–81
- Li Y, Perlman E, Wan M, Yang Y, Meneveau C, et al. 2008. A public turbulence database cluster and applications to study Lagrangian evolution of velocity increments in turbulence. *J. Turbul.* 9:N31
- Lilly DK. 1992. A proposed modification of the Germano subgrid-scale closure method. *Phys. Fluids A* 4(3):633–35
- Ling J, Kurzawski A, Templeton J. 2016. Reynolds averaged turbulence modelling using deep neural networks with embedded invariance. J. Fluid Mech. 807:155–66
- Lozano-Durán A, Holzner M, Jiménez J. 2016. Multiscale analysis of the topological invariants in the logarithmic region of turbulent channels at a friction Reynolds number of 932. *7. Fluid Mech.* 803:356–94
- Lund TS, Rogers MM. 1994. An improved measure of strain state probability in turbulent flows. *Phys. Fluids* 6(5):1838–47

- Lundgren TS. 1967. Distribution functions in the statistical theory of turbulence. Phys. Fluids 10(5):969-75
- Lundgren TS. 1982. Strained spiral vortex model for turbulent fine structure. Phys. Fluids 25(12):2193-203
- Luo Y, Shi Y, Meneveau C. 2022. Multifractality in a nested velocity gradient model for intermittent turbulence. Phys. Rev. Fluids 7:014609
- Martín J, Dopazo C, Valiño L. 1998. Dynamics of velocity gradient invariants in turbulence: restricted Euler and linear diffusion models. *Phys. Fluids* 10(8):2012–25
- Martins Afonso M, Meneveau C. 2010. Recent fluid deformation closure for velocity gradient tensor dynamics in turbulence: timescale effects and expansions. *Physica D* 239(14):1241–50
- Maxey MR. 1987. The gravitational settling of aerosol particles in homogeneous turbulence and random flow fields. 7. Fluid Mech. 174:441–65
- Meibohm J, Gustavsson K, Mehlig B. 2023. Caustics in turbulent aerosols form along the Vieillefosse line at weak particle inertia. Phys. Rev. Fluids 8:024305
- Meneveau C. 2011. Lagrangian dynamics and models of the velocity gradient tensor in turbulent flows. Annu. Rev. Fluid Mech. 43:219–45
- Meneveau C, Katz J. 2000. Scale-invariance and turbulence models for large-eddy simulation. Annu. Rev. Fluid Mech. 32:1–32
- Meneveau C, Lund TS. 1994. On the Lagrangian nature of the turbulence energy cascade. *Phys. Fluids* 6(8):2820–25
- Meneveau C, Sreenivasan KR. 1987. Simple multifractal cascade model for fully developed turbulence. *Phys. Rev. Lett.* 59(13):1424–27
- Monin AS. 1967. Equations of turbulent motion. *Prikl. Mat. Mekh.* 31(6):1057–68 (in Russian); *J. Appl. Math. Mech.* 31(6):1057–68 (English transl.)
- Moser RD, Haering SW, Yalla GR. 2021. Statistical properties of subgrid-scale turbulence models. *Annu. Rev. Fluid Mecb.* 53:255–86
- Nagata R, Watanabe T, Nagata K, da Silva CB. 2020. Triple decomposition of velocity gradient tensor in homogeneous isotropic turbulence. Comput. Fluids 198:104389
- Naso A, Pumir A. 2005. Scale dependence of the coarse-grained velocity derivative tensor structure in turbulence. *Phys. Rev. E* 72:056318
- Nelkin M. 1994. Universality and scaling in fully developed turbulence. Adv. Phys. 43(2):143-81
- Ni R, Ouellette NT, Voth GA. 2014. Alignment of vorticity and rods with Lagrangian fluid stretching in turbulence. J. Fluid Mech. 743:R3
- Novikov EA. 1967. Kinetic equations for a vortex field. *Dokl. Akad. Nauk SSSR* 177(2):299–301 (in Russian); 1968. *Sov. Phys. Dokl.* 12(11):1006–8 (English transl.)
- Oboukhov AM. 1962. Some specific features of atmospheric turbulence. 7. Fluid Mech. 13(1):77-81
- Ohkitani K, Kishiba S. 1995. Nonlocal nature of vortex stretching in an inviscid fluid. *Phys. Fluids* 7(2):411–21 Onsager L. 1949. Statistical hydrodynamics. *Nuovo Cim.* 6:279–87
- Parashar N, Srinivasan B, Sinha SS. 2020. Modeling the pressure-Hessian tensor using deep neural networks. Phys. Rev. Fluids 5:114604
- Pereira RM, Moriconi L, Chevillard L. 2018. A multifractal model for the velocity gradient dynamics in turbulent flows. 7. Fluid Mech. 839:430–67
- Pope SB. 2000. Turbulent Flows. Cambridge, UK: Cambridge Univ. Press
- Pumir A. 1994. A numerical study of pressure fluctuations in three-dimensional, incompressible, homogeneous, isotropic turbulence. Phys. Fluids 6(6):2071–83
- Richardson LF. 1922. Weather Prediction by Numerical Process. Cambridge, UK: Cambridge Univ. Press
- Schumacher J. 2007. Sub-Kolmogorov-scale fluctuations in fluid turbulence. Europhys. Lett. 80:54001
- She ZS, Jackson E, Orszag SA. 1990. Intermittent vortex structures in homogeneous isotropic turbulence. Nature 344(6263):226–28
- She ZS, Lévêque E. 1994. Universal scaling laws in fully developed turbulence. Phys. Rev. Lett. 72(3):336–39
- Siggia ED. 1981. Numerical study of small-scale intermittency in three-dimensional turbulence. *J. Fluid Mech.* 107:375–406
- Sundaram S, Collins LR. 1997. Collision statistics in an isotropic particle-laden turbulent suspension. Part 1. Direct numerical simulations. *J. Fluid Mech.* 335:75–109

- Taylor GI. 1938. Production and dissipation of vorticity in a turbulent fluid. Proc. R. Soc. A 164(916):15-23
- Tennekes H, Lumley JL. 1972. A First Course in Turbulence. Cambridge, MA: MIT Press
- Tian Y, Livescu D, Chertkov M. 2021. Physics-informed machine learning of the Lagrangian dynamics of velocity gradient tensor. Phys. Rev. Fluids 6:094607
- Tom J, Carbone M, Bragg AD. 2021. Exploring the turbulent velocity gradients at different scales from the perspective of the strain-rate eigenframe. *J. Fluid Mech.* 910:A24
- Townsend AA. 1951. On the fine-scale structure of turbulence. Proc. R. Soc. A 208(1095):534-42
- Tsinober A. 2009. An Informal Conceptual Introduction to Turbulence. Berlin: Springer
- Tsinober A, Kit E, Dracos T. 1992. Experimental investigation of the field of velocity gradients in turbulent flows. 7. Fluid Mech. 242:169–92
- van der Bos F, Tao B, Meneveau C, Katz J. 2002. Effects of small-scale turbulent motions on the filtered velocity gradient tensor as deduced from holographic particle image velocimetry measurements. *Phys. Fluids* 14(7):2456–74
- Vela-Martín A. 2022. Subgrid-scale models of isotropic turbulence need not produce energy backscatter. 7. Fluid Mech. 937:A14
- Vela-Martín A, Jiménez J. 2021. Entropy, irreversibility and cascades in the inertial range of isotropic turbulence. *J. Fluid Mech.* 915:A36
- Vieillefosse P. 1982. Local interaction between vorticity and shear in a perfect incompressible fluid. J. Phys. 43(6):837–42
- Vieillefosse P. 1984. Internal motion of a small element of fluid in an inviscid flow. Physica A 125(1):150-62
- Vlaykov DG, Wilczek M. 2019. On the small-scale structure of turbulence and its impact on the pressure field. 7. Fluid Mecb. 861:422–46
- Wallace JM. 2009. Twenty years of experimental and direct numerical simulation access to the velocity gradient tensor: What have we learned about turbulence? *Phys. Fluids* 21:021301
- Wan M, Xiao Z, Meneveau C, Eyink GL, Chen S. 2010. Dissipation-energy flux correlations as evidence for the Lagrangian energy cascade in turbulence. Phys. Fluids 22:061702
- Wilczek M, Meneveau C. 2014. Pressure Hessian and viscous contributions to velocity gradient statistics based on Gaussian random fields. *J. Fluid Mech.* 756:191–225
- Wilkinson M, Mehlig B. 2005. Caustics in turbulent aerosols. Europhys. Lett. 71(2):186–92
- Xu H, Pumir A, Bodenschatz E. 2011. The pirouette effect in turbulent flows. Nat. Phys. 7(9):709-12
- Yang PF, Zhou Z, Xu H, He G. 2023. Strain self-amplification is larger than vortex stretching due to an invariant relation of filtered velocity gradients. *J. Fluid Mech.* 955:A15
- Yeung PK, Ravikumar K. 2020. Advancing understanding of turbulence through extreme-scale computation: intermittency and simulations at large problem sizes. *Phys. Rev. Fluids* 5:110517
- Yeung PK, Zhai XM, Sreenivasan KR. 2015. Extreme events in computational turbulence. *PNAS* 112(41):12633–38